

A repeating fast radio burst source localized to a nearby spiral galaxy

<https://doi.org/10.1038/s41586-019-1866-z>

Received: 17 October 2019

Accepted: 8 November 2019

Published online: 6 January 2020

B. Marcote¹, K. Nimmo^{2,3}, J. W. T. Hessels^{2,3*}, S. P. Tendulkar^{4,5}, C. G. Bassa², Z. Paragi¹, A. Keimpema¹, M. Bhardwaj^{4,5}, R. Karuppusamy⁶, V. M. Kaspi^{4,5}, C. J. Law⁷, D. Michilli^{4,5}, K. Aggarwal^{8,9}, B. Andersen^{4,5}, A. M. Archibald^{3,10}, K. Bandura^{9,11}, G. C. Bower¹², P. J. Boyle^{4,5}, C. Brar^{4,5}, S. Burke-Spolaor^{8,9}, B. J. Butler¹³, T. Cassanelli^{14,15}, P. Chawla^{4,5}, P. Demorest¹³, M. Dobbs^{4,5}, E. Fonseca^{4,5}, U. Giri^{16,17}, D. C. Good¹⁸, K. Gourdji³, A. Josephy^{4,5}, A. Yu. Kirichenko^{19,20}, F. Kirsten²¹, T. L. Landecker²², D. Lang¹⁶, T. J. W. Lazio²³, D. Z. Li^{24,25}, H.-H. Lin²⁵, J. D. Linford¹³, K. Masui^{26,27}, J. Mena-Parra²⁸, A. Naidu^{4,5}, C. Ng¹⁴, C. Patel^{4,5}, U.-L. Pen^{14,16,25,28}, Z. Pleunis^{4,5}, M. Rafiee-Ravandi¹⁶, M. Rahman¹⁴, A. Renard¹⁴, P. Scholz^{14,22}, S. R. Siegel^{4,5}, K. M. Smith¹⁶, I. H. Stairs¹⁸, K. Vanderlinde^{14,15} & A. V. Zwaniga^{4,5}

Fast radio bursts (FRBs) are brief, bright, extragalactic radio flashes^{1,2}. Their physical origin remains unknown, but dozens of possible models have been postulated³. Some FRB sources exhibit repeat bursts^{4–7}. Although over a hundred FRB sources have been discovered⁸, only four have been localized and associated with a host galaxy^{9–12}, and just one of these four is known to emit repeating FRBs⁹. The properties of the host galaxies, and the local environments of FRBs, could provide important clues about their physical origins. The first known repeating FRB, however, was localized to a low-metallicity, irregular dwarf galaxy, and the apparently non-repeating sources were localized to higher-metallicity, massive elliptical or star-forming galaxies, suggesting that perhaps the repeating and apparently non-repeating sources could have distinct physical origins. Here we report the precise localization of a second repeating FRB source⁶, FRB 180916.J0158+65, to a star-forming region in a nearby (redshift 0.0337 ± 0.0002) massive spiral galaxy, whose properties and proximity distinguish it from all known hosts. The lack of both a comparably luminous persistent radio counterpart and a high Faraday rotation measure⁶ further distinguish the local environment of FRB 180916.J0158+65 from that of the single previously localized repeating FRB source, FRB 121102. This suggests that repeating FRBs may have a wide range of luminosities, and originate from diverse host galaxies and local environments.

The CHIME/FRB Collaboration is discovering repeating FRB sources^{5,6}, which allows subsequent targeted observations using distributed radio telescope arrays to obtain precise interferometric localizations. CHIME/FRB discovered⁶ the repeating source FRB 180916.J0158+65, which we observed with the very long baseline interferometry (VLBI) technique at a central frequency of 1.7 GHz and bandwidth of 128 MHz using eight radio telescopes of the European VLBI Network (EVN) for 5.5 h on 19 June 2019. As described in the Methods, we simultaneously recorded

both EVN single-dish raw voltage data as well as high-time-resolution intensity data using the PSRIX data recorder¹³ in filterbank mode at the 100-m Effelsberg telescope.

In a search of the PSRIX data, we detected four bursts from FRB 180916.J0158+65 with signal-to-noise ratios S/N between 9.5 and 46. The observed dispersion measures (DM) of the bursts are consistent with those previously reported⁴ for this source. The burst properties, as derived from the PSRIX data, are listed in Extended Data Table 1.

¹Joint Institute for VLBI ERIC (JIVE), Dwingeloo, The Netherlands. ²ASTRON, Netherlands Institute for Radio Astronomy, Dwingeloo, The Netherlands. ³Anton Pannekoek Institute for Astronomy, University of Amsterdam, Amsterdam, The Netherlands. ⁴Department of Physics, McGill University, Montréal, Québec, Canada. ⁵McGill Space Institute, McGill University, Montréal, Québec, Canada. ⁶Max-Planck-Institut für Radioastronomie, Bonn, Germany. ⁷Department of Astronomy and Owens Valley Radio Observatory, California Institute of Technology, Pasadena, CA, USA. ⁸Department of Physics and Astronomy, West Virginia University, Morgantown, WV, USA. ⁹Center for Gravitational Waves and Cosmology, West Virginia University, Chestnut Ridge Research Building, Morgantown, WV, USA. ¹⁰School of Mathematics, Physics, and Statistics, University of Newcastle, Newcastle upon Tyne, UK. ¹¹Lane Department of Computer Science and Electrical Engineering, Morgantown, WV, USA. ¹²Academia Sinica Institute of Astronomy and Astrophysics, Hilo, HI, USA. ¹³National Radio Astronomy Observatory, Socorro, NM, USA. ¹⁴Dunlap Institute for Astronomy and Astrophysics, University of Toronto, Toronto, Ontario, Canada. ¹⁵Department of Astronomy and Astrophysics, University of Toronto, Toronto, Ontario, Canada. ¹⁶Perimeter Institute for Theoretical Physics, Waterloo, Ontario, Canada. ¹⁷Department of Physics and Astronomy, University of British Columbia, Vancouver, British Columbia, Canada. ¹⁸Instituto de Astronomía, Universidad Nacional Autónoma de México, Ensenada, Baja California, Mexico. ¹⁹Ioffe Institute, St Petersburg, Russia. ²⁰Department of Space, Earth and Environment, Chalmers University of Technology, Onsala Space Observatory, Onsala, Sweden. ²²Dominion Radio Astrophysical Observatory, Herzberg Astronomy and Astrophysics Research Centre, National Research Council Canada, Penticton, British Columbia, Canada. ²³Jet Propulsion Laboratory, California Institute of Technology, Pasadena, CA, USA. ²⁴Department of Physics, University of Toronto, Toronto, Ontario, Canada. ²⁵Canadian Institute for Theoretical Astrophysics, Toronto, Ontario, Canada. ²⁶MIT Kavli Institute for Astrophysics and Space Research, Massachusetts Institute of Technology, Cambridge, MA, USA. ²⁷Department of Physics, Massachusetts Institute of Technology, Cambridge, MA, USA. ²⁸Canadian Institute for Advanced Research, CIFAR Program in Gravitation and Cosmology, Toronto, Ontario, Canada. *e-mail: J.W.T.Hessels@uva.nl

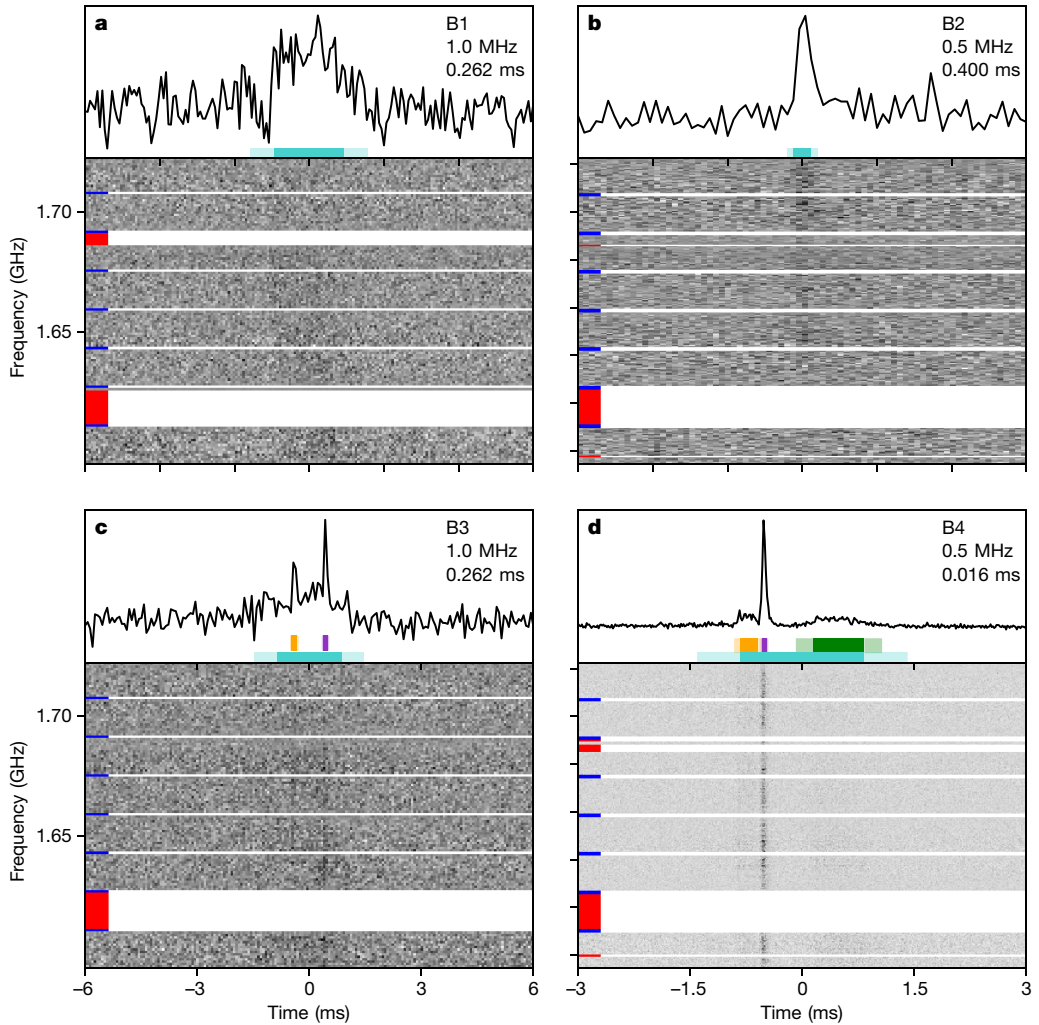


Fig. 1 | Burst detections in Effelsberg auto-correlation data. Band-averaged profiles and dynamic spectra of the four bursts, as detected using the coherently dedispersed Effelsberg auto-correlation data (**a**, **b**, **c** and **d**). Each burst was fitted with a Gaussian distribution to determine the full-width at half-maximum (FWHM) durations, which are represented by the dark cyan bars. The lighter cyan encloses the 2σ region. Bursts B3 and B4 (**c** and **d**) show sub-bursts; the orange, purple and green bars correspond to the FWHM of these sub-bursts, and the lighter bar (of each colour) encloses the 2σ region. Note the

different time windows plotted: B1 and B3 (**a** and **c**) show 12 ms, whereas B2 and B4 (**b** and **d**) show 6 ms surrounding the burst peak. The solid white lines represent frequency channels that have been removed from the data due to either radio frequency interference (RFI) or subband edges, indicated by the red and blue markers, respectively. The burst data have been downsampled by various factors in time and frequency to optimize the visual representation. The RFI excision was done before downsampling. The time and frequency resolution used for plotting is shown in the top right of each panel.

No other dispersed single pulses of plausible astrophysical origin were found in this search, for DMs in the range 0 – 700 pc cm $^{-3}$. Using the EVN raw voltage data, we generated high-time-resolution (16- μ s samples) Effelsberg auto-correlation data containing each burst. We used coherent dedispersion to mitigate the intra-channel smearing that dominated over the temporal resolution in the PSRIX data. By minimizing dispersion broadening, we properly resolve the burst structure, and find a best-fit DM = 348.76 ± 0.10 pc cm $^{-3}$ using the brightest burst (Methods). We also detect brightness modulation with a characteristic frequency scale of 59 ± 13 kHz, which we interpret as scintillation imparted by the ionized interstellar medium of the Milky Way (Methods). The properties of the four bursts, as seen in the Effelsberg auto-correlations, are also shown in Extended Data Table 1. The frequency-averaged burst profiles and dedispersed dynamic spectra are shown in Fig. 1 and Extended Data Fig. 1 for the Effelsberg auto-correlation and PSRIX data, respectively.

We then used the EVN raw voltage data to create coherently dedispersed cross-correlations, also known as visibilities, at the times of the four bursts. Radio interferometric images with milli-arcsecond resolution were produced for each individual burst, using a single 0.7–2.7-ms

integration, depending on the burst duration. Each image shows emission above at least seven times the root-mean-square (r.m.s.) noise level (Fig. 2; see Methods for a detailed explanation of the calibration and imaging process). The four burst images provide an average J2000 position for FRB180916.J0158+65 of $\alpha = 01^{\text{h}} 58^{\text{m}} 00.75017^{\text{s}} \pm 2.3^{\text{mas}}$, $\delta = 65^{\circ} 43' 00.3152'' \pm 2.3^{\text{mas}}$. Visibilities with 2-s time resolution were also generated for the entire observation span. We used these to produce an image of the field around FRB180916.J0158+65 in order to search for a persistent radio counterpart, like that seen in the case of FRB121102^{9,14}. No such emission is detected above a 3 σ r.m.s. noise level of 30 μ Jy per beam. Independent observations using the Karl G. Jansky Very Large Array (VLA) at 1.6 GHz detect no coincident emission above a 3 σ r.m.s. noise level of 18 μ Jy per beam (see Methods and Extended Data Fig. 2).

The precise EVN position shows that FRB180916.J0158+65 is spatially coincident with a galaxy catalogued in the Sloan Digital Sky Survey¹⁵ as SDSSJ015800.28+654253.0. Given the maximum expected redshift of approximately 0.11, as inferred by the measured DM (Methods), we find that the probability for chance coincidence is less than 1% for any type of galaxy with mass greater than about 40% that of the FRB121102

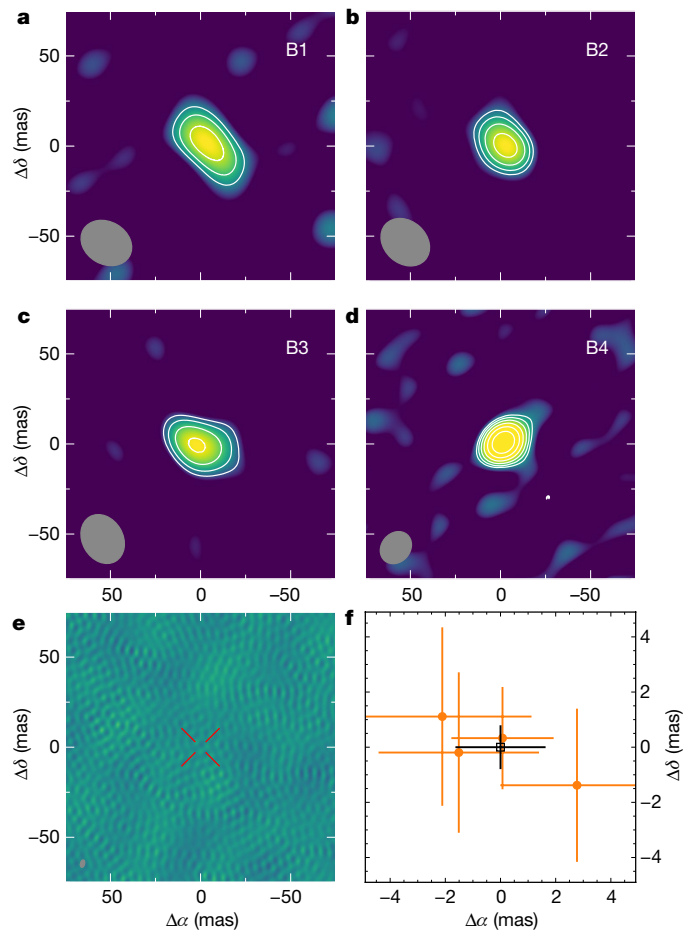


Fig. 2 | EVN images and burst positions. Each individual burst is imaged by using the EVN gated visibility data (**a**, **b**, **c** and **d**). **e**, Image using the full span of the EVN observation and 2-s integration time; no significant ($>3\sigma$) persistent radio emission is detected at the positions of the bursts (denoted by the red cross) and no signal above the 4σ level is detected anywhere within the full field. Contours start at three times the r.m.s. noise level of each image (75 mJy per beam, 65 mJy per beam, 43 mJy per beam and 100 mJy per beam and 9.7 μJy per beam, respectively) and increase by factors of $\sqrt{2}$. For all images, the synthesized beam is represented by the grey ellipse in the bottom-left corner. The Tianma station was only included in the derivation of the continuum image (**e**). **f**, The positions derived from each individual burst and their associated 1σ uncertainties (orange), with respect to the weighted-average burst position (black). All positions are referenced to right ascension α (J2000) = 01 h 58 min 00.75017 s, declination δ (J2000) = 65° 43' 00.3152".

host (Methods). Moreover, we thus conclude that the association of FRB 180916.J0158+65 to this particular galaxy is well established. FRB 180916.J0158+65 is close to the plane of the Milky Way, with Galactic longitude $l=129.7^\circ$ and latitude $b=3.7^\circ$. Its low DM excess compared to the Milky Way contribution (Methods) brought into question whether it could possibly be a Galactic disk or halo object⁶, but the host galaxy association shows that it is clearly extragalactic.

We used the 8-m Gemini-North telescope to characterize the morphology of the host galaxy and to measure a spectroscopic redshift (Methods). Deep optical imaging reveals that the host is a nearly face-on spiral galaxy (Fig. 3) with a total stellar mass of approximately 10^{10} times that of the Sun (Methods), which is comparable to the total stellar mass of the Milky Way. No other comparably large and bright galaxy is visible in the broader field covered by Gemini-North (Extended Data Fig. 3). The milli-arcsecond precision of the EVN localization shows that the FRB source is close to a bright feature in the r' -band approximately 7 arcsec (projected separation of roughly 4.7 kpc) from the core of the host galaxy.

With Gemini-North long-slit spectroscopy, we simultaneously targeted the host galaxy centre and the offset position of FRB 180916.J0158+65 (Extended Data Fig. 3). This revealed strong H α emission, and several other spectral lines frequently associated with star formation (Fig. 3). By measuring optical line ratios, we confirm that the host is indeed a star-forming galaxy (Extended Data Fig. 5).

Comparing with the rest frequencies of the lines, we find a redshift $z=0.0337 \pm 0.0002$, which corresponds to a luminosity distance of 149.0 ± 0.9 Mpc (or an angular size distance of 139.4 ± 0.8 Mpc) using standard cosmological parameters¹⁶. FRB 180916.J0158+65 is thus the closest-known FRB source with a robust host galaxy identification and measured redshift. It is a factor of six closer than the repeater FRB 121102¹⁷, and more than an order-of-magnitude closer than the (thus far) non-repeating sources FRB 180924¹¹, FRB 181112¹² and FRB 190523¹⁰.

The optical spectrum at the location of FRB 180916.J0158+65 shows that both the associated star-forming clump and the host galaxy core are at the same redshift (Fig. 3). However, the spectrum at the location of FRB 180916.J0158+65 is dominated by emission from the clump, which is offset from the centre of the slit. Hence we have no independent direct estimate of the emission or dispersion measure at the position of FRB 180916.J0158+65 from the Gemini-North data. By considering the various modelled foreground contributions to DM, we estimate that the host contribution is less than approximately 70 pc cm^{-3} , and could be substantially smaller (Methods).

FRB 180916.J0158+65 is located at the apex of the v-shaped star-forming clump (Extended Data Fig. 4) with a relatively large¹⁸ projected size of roughly 1.5 kpc and a star-formation rate of greater than about $0.016 M_\odot \text{ yr}^{-1}$ (and a star-formation surface density of about $10^{-2} M_\odot \text{ yr}^{-1} \text{ kpc}^{-2}$). The v-shaped star-forming clump is a remarkable feature of the galaxy, suggesting the possibility that the region has undergone an interaction that triggered the star formation, either between multiple star-forming regions or conceivably involving a putative dwarf satellite companion.

The spiral host galaxy of FRB 180916.J0158+65 contains over 100 times more stellar mass and has a metallicity five times higher (see Extended Data Fig. 5 and Methods) than the dwarf host galaxy of FRB 121102. The discovery of this host demonstrates that some FRB sources exist in galaxies more similar to our own Milky Way. Previously, it has been noted^{14,17,19} that the host of FRB 121102 is similar to the type of low-metallicity galaxies with high specific star-formation rate that are associated with hydrogen-poor superluminous supernovae and long-duration gamma-ray bursts. In contrast, the FRB 180916.J0158+65 host is unlike such galaxies; this weakens the case for a general link between all repeating FRB sources and these extreme astrophysical explosions. In a search of the Open Supernova Catalog²⁰, we find no previous supernovae or gamma-ray bursts at the location of FRB 180916.J0158+65.

The proximity of FRB 180916.J0158+65 constrains the presence of any persistent radio counterpart to a luminosity (at a 3σ confidence level) of $vL_v < 1.3 \times 10^{36} \text{ erg s}^{-1}$ from the continuum EVN data (sensitive to milli-arcsecond scales) and to $vL_v < 7.6 \times 10^{35} \text{ erg s}^{-1}$ from the VLA data (sensitive to emission on arcsecond scales; see Methods). Compared to the persistent source associated with the repeating FRB 121102, this upper limit implies that any such source associated with FRB 180916.J0158+65 must be at least 400 times fainter than the one associated with FRB 121102¹⁴. The previously determined⁶ Faraday rotation measure (RM) of FRB 180916.J0158+65, $\text{RM} = -114.6 \pm 0.6 \text{ rad m}^{-2}$, is three orders of magnitude lower than that of FRB 121102²¹, where $\text{RM} \approx 10^5 \text{ rad m}^{-2}$. As previously suggested⁶, we conclude that FRB 180916.J0158+65 is located in a much less extreme local environment compared with FRB 121102, and that the physical mechanism for FRB repetition does not depend on such conditions. Nonetheless, models originally proposed for FRB 121102^{22,23}—in which the bursts originate from a young and rapidly rotating magnetar—could potentially still explain the observed properties of FRB 180916.J0158+65 by invoking an age of approximately 300 yr, which is ten times older than that proposed for FRB 121102 (see Methods for a brief comparison to existing models).

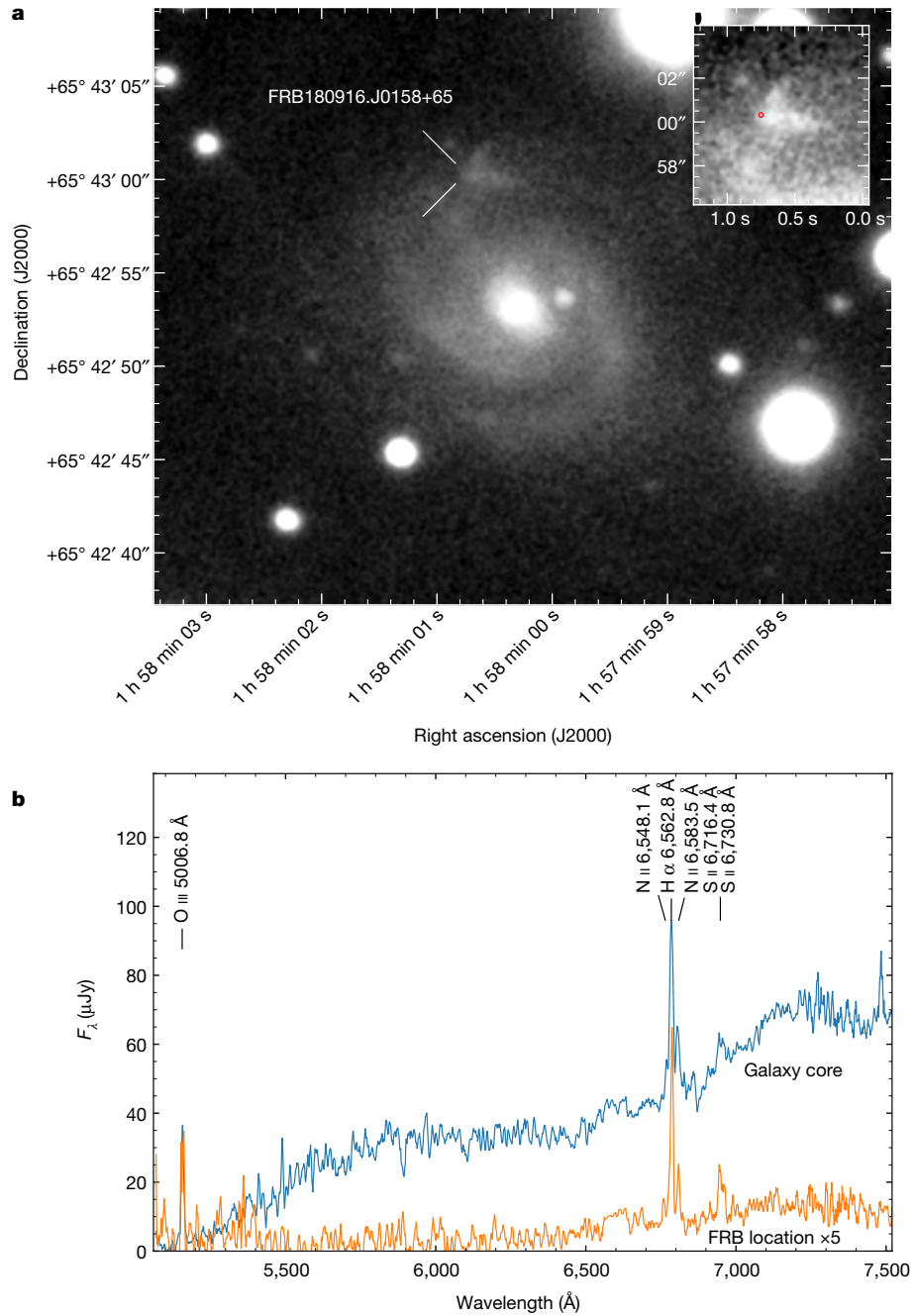


Fig. 3 | Gemini-North host galaxy image and optical spectrum. **a**, Image of the host galaxy using the r' filter. The position of FRB180916.J0158+65 is marked. The inset shows a higher-contrast zoom-in of the star-forming region containing FRB180916.J0158+65 (marked by the red circle). The uncertainty in the position of FRB180916.J0158+65 is smaller than the resolution of the image. **b**, Sky-subtracted spectrum extracted from a 5-arcsec aperture around

the host galaxy core (blue) and a 2-arcsec aperture around the location of FRB180916.J0158+65 (orange, scaled by a factor of five for clarity). Emission lines are identified along with their rest-frame wavelengths in air. Owing to the complicated shape of the galaxy, the flux densities, F_λ , have not been corrected for slit losses.

Although the host galaxies of FRB180916.J0158+65 and FRB121102 are markedly different, both sources are located near or within a star-forming region in the host galaxy. This contrasts with the elliptical host galaxies of FRB180924¹¹ and FRB190523¹⁰, where there is comparatively little active star formation, but may be consistent with the star-forming galaxy of FRB181112¹². This diversity in hosts and local environments allows for the possibility that repeating and apparently non-repeating FRB sources have physically distinct origins. However, comparison of FRB event rates with those of proposed progenitors disfavours models that invoke cataclysmic explosions and suggests

that a large fraction of sources must be capable of repeating²⁴. The recent finding that FRB171019 produces repeat bursts that are almost 600 times fainter than the originally discovered signal⁷ underscores the fact that the detectability of repetition depends on instrumental sensitivity and source proximity. If FRB180916.J0158+65 were at the distance of the other well localized FRBs, only a small fraction of its (brightest) bursts would be visible.

Furthermore, it has been proposed that a young magnetar origin for the bursts of as-yet non-repeating FRBs in non-star-forming regions is still viable as long as it is possible to form such sources through a variety

Table 1 | Burst properties

Burst	W_{tot} (ms)	W_{sub1} (ms)	W_{sub2} (ms)	W_{sub3} (ms)	Fluence (Jy ms) ^a	Spectral energy density (10^{28} erg Hz ⁻¹) ^a	$\Delta\alpha$ (mas)	$\Delta\delta$ (mas)	S_v (Jy) ^b
B1	1.86 ± 0.13	–	–	–	0.72	1.90	-2.1 ± 3.2	1.1 ± 3.2	0.74 ± 0.08
B2	0.24 ± 0.02	–	–	–	0.20	0.53	-1.5 ± 2.9	-0.2 ± 2.9	0.66 ± 0.05
B3	1.72 ± 0.14	0.14 ± 0.02	0.12 ± 0.01	–	0.62	1.64	2.8 ± 2.8	-1.4 ± 2.8	0.50 ± 0.04
B4	1.66 ± 0.05^c	0.24 ± 0.01	0.06 ± 0.0006	0.68 ± 0.03	2.53	6.68	0.1 ± 1.9	0.3 ± 1.9	2.3 ± 0.3

Widths, fluences and spectral energy densities are determined using the Effelsberg auto-correlation data of the bursts from FRB 180916.J0158+65, with a centre frequency of 1.7 GHz and dedispersed for a DM = 348.76 pc cm⁻³. W_{tot} is the FWHM of the total burst envelope, and W_{subn} represents the FWHM of any sub-bursts, ordered according to their arrival time (the earliest sub-burst is labelled ‘sub1’). The fluence is determined by integrating the burst profile over W_{tot} and is converted to physical units using the radiometer equation³⁴ (see Methods). The spectral energy density is estimated using the measured fluence and luminosity distance. The position offsets ($\Delta\alpha$, $\Delta\delta$) are referred to the average J2000 burst position of $\alpha = 01^\circ h 58^\circ m 00.75017^\circ s$, $\delta = +65^\circ 43' 00.3152''$. The flux densities S_v are measured by fitting a circular Gaussian to the EVN visibility data and are averages over the gate width.

^aAt 1.7-GHz reference frequency, and corresponding to the sum of all sub-bursts. A conservative fractional error of 30% is adopted for the derived fluences and energy densities. These are assumed to be isotropic.

^bAt 1.7-GHz reference frequency. The absolute flux scale may exhibit an additional ~15% uncertainty due to possible systematic gain calibration offsets.

^cSee Methods for how the total burst width of B4 was determined.

of channels, including direct stellar collapse, accretion-induced collapse, and through the merger of compact objects²⁵. Ultimately, a larger number of precision localizations is needed before we can establish that multiple physical origins are required to explain the observed FRB phenomenon. There are now 11 repeating FRBs published^{4–7}, and with precision localizations it will be possible to establish whether repeating and apparently non-repeating FRB sources have demonstrably different environments.

FRBs have now been localized with luminosity distances that span approximately 150 Mpc to 4 Gpc. Estimating distance purely based on DM, it appears likely that there are FRBs that are even closer²⁶ or more distant²⁷ compared with this range. The four bursts presented here have isotropic-equivalent spectral energy densities as low as approximately 5×10^{-27} erg Hz⁻¹ (Table 1). Assuming similar beaming fractions, this makes them close to an order of magnitude less energetic than the weakest bursts seen from FRB 121102 to date²⁸, and between four to six orders-of-magnitude less energetic than FRB 180924¹¹ and FRB 190523¹⁰. Unless multiple models are invoked, a viable model for FRBs must address this large range of (apparent) energy outputs.

Comparing instead with pulsar emission, we note that the bursts from FRB 180916.J0158+65 are still at least a million times more energetic than the brightest giant pulses seen from the Crab pulsar—suggesting that they are not simply an exceptionally bright version of the known pulsar giant pulse phenomenon²⁹.

As previously suggested⁶, the proximity of FRB 180916.J0158+65 is an advantage for multi-wavelength follow-up of the host galaxy and local environment. Whereas targeted observations of FRB 121102 have failed to detect either prompt or persistent optical, X-ray or gamma-ray counterparts^{30–33}, similar observations towards FRB 180916.J0158+65 may strongly constrain magnetar-based models, even in the event of non-detections. FRB 180916.J0158+65 is thus one of the most promising known sources for understanding the nature of FRBs.

Online content

Any methods, additional references, Nature Research reporting summaries, source data, extended data, supplementary information, acknowledgements, peer review information; details of author contributions and competing interests; and statements of data and code availability are available at <https://doi.org/10.1038/s41586-019-1866-z>.

- Lorimer, D. R., Bailes, M., McLaughlin, M. A., Narkevic, D. J. & Crawford, F. A bright millisecond radio burst of extragalactic origin. *Science* **318**, 777–780 (2007).
- Petroff, E., Hessels, J. W. T. & Lorimer, D. R. Fast radio bursts. *Astron. Astrophys. Rev.* **27**, 4 (2019).
- Platts, E. et al. A living theory catalogue for fast radio bursts. *Phys. Rep.* **821**, 1–27 (2019).
- Spitler, L. G. et al. A repeating fast radio burst. *Nature* **531**, 202–205 (2016).
- CHIME/FRB Collaboration. A second source of repeating fast radio bursts. *Nature* **566**, 235–238 (2019).

- The CHIME/FRB Collaboration. CHIME/FRB discovery of eight new repeating fast radio burst sources. *Astrophys. J.* **885**, L24 (2019).
- Kumar, P. et al. Faint repetitions from a bright fast radio burst source. Preprint at <https://arxiv.org/abs/1908.10026> (2019).
- Petroff, E. et al. FRBCAT: The Fast Radio Burst Catalogue. *Publ. Astron. Soc. Aust.* **33**, e045 (2016).
- Chatterjee, S. et al. A direct localization of a fast radio burst and its host. *Nature* **541**, 58–61 (2017).
- Ravi, V. et al. A fast radio burst localized to a massive galaxy. *Nature* **572**, 352–354 (2019).
- Bannister, K. W. et al. A single fast radio burst localized to a massive galaxy at cosmological distance. *Science* **365**, 565–570 (2019).
- Prochaska, J. X. et al. The low density and magnetization of a massive galaxy halo exposed by a fast radio burst. *Science* **366**, 231–234 (2019).
- Lazarus, P. et al. Prospects for high-precision pulsar timing with the new Effelsberg PSRIX backend. *Mon. Not. R. Astron. Soc.* **458**, 868–880 (2016).
- Marcote, B. et al. The repeating fast radio burst FRB 121102 as seen on milliarcsecond angular scales. *Astrophys. J.* **834**, L8 (2017).
- Alam, S. et al. The eleventh and twelfth data releases of the Sloan Digital Sky Survey: final data from SDSS-III. *Astrophys. J. Suppl.* **219**, 12 (2015).
- Wright, E. L. A cosmology calculator for the world wide web. *Publ. Astron. Soc. Pacif.* **118**, 1711–1715 (2006).
- Tendulkar, S. P. et al. The host galaxy and redshift of the repeating fast radio burst FRB 121102. *Astrophys. J.* **834**, L7 (2017).
- Gusev, A. S. Hierarchy and size distribution function of star formation regions in the spiral galaxy NGC 628. *Mon. Not. R. Astron. Soc.* **442**, 3711–3721 (2014).
- Metzger, B. D., Berger, E. & Margalit, B. Millisecond magnetar birth connects FRB 121102 to superluminous supernovae and long-duration gamma-ray bursts. *Astrophys. J.* **841**, 14 (2017).
- Guillochon, J., Parrent, J., Kelley, L. Z. & Margutti, R. An open catalog for supernova data. *Astrophys. J.* **835**, 64 (2017).
- Michilli, D. et al. An extreme magneto-ionic environment associated with the fast radio burst source FRB 121102. *Nature* **553**, 182–185 (2018).
- Margalit, B. & Metzger, B. D. A concordance picture of FRB 121102 as a flaring magnetar embedded in a magnetized ion-electron wind nebula. *Astrophys. J.* **868**, L4 (2018).
- Metzger, B. D., Margalit, B. & Sironi, L. Fast radio bursts as synchrotron maser emission from decelerating relativistic blast waves. *Mon. Not. R. Astron. Soc.* **485**, 4091–4106 (2019).
- Ravi, V. The prevalence of repeating fast radio bursts. *Nat. Astron.* **3**, 928–931 (2019).
- Margalit, B., Berger, E. & Metzger, B. D. Fast radio bursts from magnetars born in binary neutron star mergers and accretion induced collapse. *Astrophys. J.* **886**, 110 (2019).
- Mahony, E. K. et al. A search for the host galaxy of FRB 171020. *Astrophys. J.* **867**, L10 (2018).
- Bhandari, S. et al. The survey for pulsars and extragalactic radio bursts. II. New FRB discoveries and their follow-up. *Mon. Not. R. Astron. Soc.* **475**, 1427–1446 (2018).
- Gourdji, K. et al. A sample of low-energy bursts from FRB 121102. *Astrophys. J.* **877**, L19 (2019).
- Lyutikov, M. Fast radio bursts’ emission mechanism: implication from localization. *Astrophys. J.* **838**, L13 (2017).
- Scholz, P. et al. The repeating fast radio burst FRB 121102: multi-wavelength observations and additional bursts. *Astrophys. J.* **833**, 177 (2016).
- Scholz, P. et al. Simultaneous X-ray, gamma-ray, and radio observations of the repeating fast radio burst FRB 121102. *Astrophys. J.* **846**, 80 (2017).
- Hardy, L. K. et al. A search for optical bursts from the repeating fast radio burst FRB 121102. *Mon. Not. R. Astron. Soc.* **472**, 2800–2807 (2017).
- MAGIC Collaboration. Constraining very-high-energy and optical emission from FRB 121102 with the MAGIC telescopes. *Mon. Not. R. Astron. Soc.* **481**, 2479–2486 (2018).
- Cordes, J. M. & McLaughlin, M. A. Searches for fast radio transients. *Astrophys. J.* **596**, 1142–1154 (2003).

Publisher’s note Springer Nature remains neutral with regard to jurisdictional claims in published maps and institutional affiliations.

© The Author(s), under exclusive licence to Springer Nature Limited 2020

Methods

A priori localization

The CHIME/FRB Collaboration discovered⁶ the repeating source FRB 180916.J0158+65 and refined its position using the CHIME/FRB baseband mode. The automatic baseband triggering system of CHIME/FRB³⁵ captured⁶ raw voltages for a burst from FRB 180916.J0158+65. The intensity of the signal in the region surrounding the original detection was then calculated by producing a grid of tightly packed tied-array beams. A refined position was obtained by fitting this intensity map with a simple model of the telescope beam. The technique will be described in more detail in a future paper (D.M. et al., manuscript in preparation). Since the analysis strategy was still in a preliminary stage at the time, we estimate a systematic uncertainty on this position of roughly 3 arcmin, based on a small sample of four known pulsars. CHIME/FRB baseband localizations are expected to have higher precision in the future.

European VLBI Network and Effelsberg observations

The EVN observed the field of FRB 180916.J0158+65 on 19 June 2019 for 5.5 h at a central frequency of 1.7 GHz and with a bandwidth of 128 MHz. The phase centre was placed at the position provided by the initial CHIME/FRB baseband localization: $\alpha = 01^{\text{h}} 57^{\text{m}} 43.2^{\text{s}}$, $\delta = 65^{\circ} 42' 01.02''$ (J2000 coordinates).

A total of eight dishes participated in the EVN observations: the 100-m Effelsberg, the 65-m Tianma, the 32-m Medicina, the 32-m Toruń, the 32-m Irbene, the 25-m \times 38-m Jodrell Bank Mark II, the 25-m Onsala, and a single 25-m dish from the Westerbork array. The data were streamed in real time (e-EVN setup) to the EVN Software Correlator (SFXC³⁶) at the Joint Institute for VLBI ERIC (JIVE) in Dwingeloo, The Netherlands. The real-time visibility data are comprised of eight 16-MHz subbands of 32 channels each, with full circular polarization products, and 2-s time averaging.

In parallel, we buffered the individual station raw voltage data in order to allow high-time-resolution correlations afterwards, at the times of any detected bursts. This method allows one to recover the signal from any position within the primary beam of the antennas (which have a full-width at half-maximum, FWHM, of roughly 7 arcmin in the case of the 100-m Effelsberg dish, and roughly 30 arcmin for the 25-m antennas), which would otherwise be smeared due to time and frequency averaging if it is more than tens of arcseconds away from the phase centre used in cross-correlation. We observed 3C454.3 and J0745+1011 as fringe-finders and bandpass calibrators. J0207+6246 was observed as phase calibrator (located 3.1° away from FRB 180916.J0158+65) in a phase-referencing cycle of 2 min on the calibrator and 5 min on the target, FRB 180916.J0158+65. We also observed J0140+6346 as a check source (3.1° away from the same phase calibrator) following the same phase-referencing cycle.

Simultaneously, we recorded high-time-resolution filterbank data at 1.7 GHz using the 100-m Effelsberg telescope and the PSRIX data recorder¹³, which is designed for pulsar observations. We observed FRB 180916.J0158+65 for a total on-source time of 3.47 h in the frequency range 1597–1737 MHz. This total bandwidth was divided into 144 spectral channels of 0.98 MHz each. Of these, the bottom 48 channels were corrupted by RFI, probably from Iridium satellites. Consequently, these channels were removed from the data before beginning the analysis, giving a usable bandwidth of 93.75 MHz. The data were recorded with full Stokes information and a time resolution of 81.92 μ s. Before the beginning of the observation, we performed a short test scan on the known pulsar PSR B2111+46, to verify the data integrity.

Interferometric data reduction

The EVN data were analysed using standard procedures within the Astronomical Image Processing System (AIPS³⁷) and Difmap³⁸ software packages. A priori amplitude calibration was performed using the known gain curves and system temperature measurements recorded

at each station during the observations. Poor data, primarily due to RFI, were flagged manually (less than about 10% of the total data). The remaining data were then fringe-fitted and bandpass calibrated using the fringe-finders and phase calibrator, which were imaged and self-calibrated to improve the final calibration of the data. The obtained solutions were transferred to FRB 180916.J0158+65 and J0140+6346 before creating the final images.

The check source J0140+6346 was used to estimate both the absolute astrometric uncertainty and the potential amplitude losses that could have been introduced due to the phase-referencing technique. Although the latter accounted for less than approximately 10% of the total flux density scale, we found a larger-than-expected offset (about 4 mas) of the centroid of the check source position with respect to its known coordinates from the International Celestial Reference Frame. The origin of this offset is explained by both the uncertainties associated with the phase-referencing technique^{39–41} and the extended structure of J0207+6246, the phase calibrator. The core of this source shows multiple components that make the determination of the true position of the source ambiguous at the milli-arcsecond level. We corrected for this observed offset in all burst positions presented in this study, but an uncertainty on the final absolute positions of ± 1.7 mas and ± 2.1 mas in right ascension and declination, respectively, still remains owing to the ambiguity in the exact position of this reference source and its extension (the source is resolved on milli-arcsecond scales).

Search for FRB 180916.J0158+65 bursts

The PSRIX data were analysed in order to search for dispersed, millisecond-duration bursts, using the PRESTO⁴² software package. The tool *rffifind* was used to identify frequency channels and time samples contaminated by RFI. We estimate that ~4% of the data were masked using *rffifind*. Incorporating the RFI mask, the data were then incoherently dedispersed to DMs in the range 0–700 pc cm⁻³ in steps of 1 pc cm⁻³ using *presubband*, generating dedispersed time series at each trial DM. To search for short-duration bursts, each dedispersed time series was convolved with boxcar functions of various widths, using *single_pulse_search.py*. Given the frequency resolution of the PSRIX data, the residual dispersive delay within each channel results in a temporal smearing of about 0.6 ms at the expected⁶ DM of FRB 180916.J0158+65 (349 pc cm⁻³). This intra-channel smearing dominates over the sampling time, causing a loss of sensitivity to extremely narrow bursts. We were sensitive to bursts with widths exceeding the intra-channel smearing time and up to 98.3 ms. A DM-versus-time plot (known as a single-pulse plot, generated by *single_pulse_search.py*) was created for each scan and inspected by eye for candidates. For each candidate identified, the dynamic spectrum was generated and inspected by eye to distinguish between astrophysical signals and terrestrial sources of RFI. During our 3.47-h on-source time, we found four bursts from FRB 180916.J0158+65 at its known DM. As a final check, each dedispersed time series was filtered for RFI in the search for candidates with peak $S/N > 7$, using an automated classifier^{43,44} that returned only the same four bursts found in the initial manual search.

Using the time of arrival of each individual burst, one-second-duration Effelsberg auto-correlations were created for each burst, using the recorded EVN raw-voltage data. The auto-correlation data were generated with a higher temporal resolution (16- μ s time bins) and frequency resolution (62.5-kHz channels) compared with the PSRIX data, and were coherently dedispersed to 350 pc cm⁻³. Coherent dedispersion mitigates the effects of intra-channel smearing to less than 3 μ s for DMs that are within a few units of 350 pc cm⁻³. This provided us with the opportunity to better study the burst structure (limited only by our temporal resolution and the S/N), which is unresolved in the PSRIX data.

We identified the four bursts from FRB 180916.J0158+65 in the auto-correlations (Fig. 1 shows their band-averaged burst profiles and dynamic spectra). For comparison, we also show the profiles and dynamic spectra for the bursts in the PSRIX data (Extended Data Fig. 1).

Article

Burst properties

Using the brightest burst, labelled B4, we determined a precise DM for FRB 180916.J0158+65. We used the PSRCHIVE⁴⁵ tool *pdmp* to determine the DM that corresponds to a peak in the *S/N*. Because B4 has a bright and narrow sub-burst, optimizing the *S/N* is probably also equivalent to optimizing the structure of the burst⁴⁶, in this case. We searched DMs of $350 \pm 3 \text{ pc cm}^{-3}$ in steps of 0.01 pc cm^{-3} using *pdmp*, and found the optimal DM to be $348.76 \pm 0.10 \text{ pc cm}^{-3}$ (consistent with the DM of $349.2 \pm 0.3 \text{ pc cm}^{-3}$ determined for this source by CHIME/FRB⁶). The bursts shown in both Fig. 1 and Extended Data Fig. 1 are dedispersed to this DM value.

Table 1 lists the physical properties of the bursts using the Effelsberg auto-correlations, dedispersed to $348.76 \text{ pc cm}^{-3}$. We measured the burst FWHM duration and peak time using a Gaussian fit⁴⁶. The brightest burst, B4, shows a complicated structure (as can be seen in Fig. 1). The width of each individual sub-burst in B4 was determined using the same Gaussian fit as above. The total width of B4, however, was measured by defining the beginning of the burst as the peak time of the first sub-burst minus half $W_{\text{sub}1}$, and the end of the burst as the peak time of the last sub-burst plus half $W_{\text{sub}3}$.

To determine the fluence, we define a larger time window, determined by eye, than the quoted FWHM durations, which encompasses all of the burst flux. First, we produce a time series containing each burst by summing over all frequency channels. We define an off-pulse region, and use this to normalize the time series. We then convert the signal in each time bin to physical units by using the radiometer equation³⁴, and sum over the burst duration to estimate the fluence. It should be noted that B1 and B3 were downsampled by a factor of four for this analysis, resulting in a lower time resolution than the other bursts. For the radiometer equation, we take typical values for the system temperature $T_{\text{sys}} \approx 20 \text{ K}$ and telescope gain $G \approx 1.54 \text{ KJy}^{-1}$ for Effelsberg. For the fluence values quoted in Table 1, we provide a conservative fractional error of 30%. Also shown in Table 1 are the burst spectral energy densities⁴⁷, using the derived burst fluences and luminosity distance to FRB 180916.J0158+65. All four bursts are much dimmer than those previously detected⁶ with CHIME/FRB, which is unsurprising given the higher sensitivity of the 100-m Effelsberg telescope.

Extended Data Table 1 shows the detection properties of the bursts, as seen in both the PSRIX data and the Effelsberg auto-correlations. For the PSRIX data, we quote the maximum *S/N* detected using PRESTO's *single_pulse_search.py* with an associated DM. The burst *S/N* for the auto-correlations is that measured at $\text{DM} = 348.76 \text{ pc cm}^{-3}$, again using *single_pulse_search.py*. The burst width in Extended Data Table 1 is the boxcar width used in *single_pulse_search.py* resulting in the peak *S/N* value. The *S/N* of the four bursts, as discovered in the PSRIX data, are shown in Extended Data Fig. 6 as a function of time during our observation. The first three bursts appear clustered in time, occurring within 1.5 h of the beginning of our observation.

To study frequency-dependent brightness variations in the dominant sub-burst of B4—which are expected if there is scintillation—we conducted a standard auto-correlation analysis⁴⁸. We generated the spectrum of the burst within the FWHM duration ($W_{\text{sub}2} = 0.06 \text{ ms}$) using Effelsberg auto-correlations with a frequency resolution of 15.6 kHz. Spectral channels containing substantial RFI, along with those at the edges of the 16-MHz subbands, were set to zero in the spectrum before generating the auto-correlation function (ACF).

We calculated the ACF using the following expression:

$$\text{ACF}(\Delta\nu) = \frac{\sum_i (S(v_i) - \bar{S})(S(v_i + \Delta\nu) - \bar{S})}{\sqrt{\sum_i (S(v_i) - \bar{S})^2} \sqrt{\sum_i (S(v_i + \Delta\nu) - \bar{S})^2}} \quad (1)$$

where v is the frequency, $\Delta\nu$ is the frequency lag, and \bar{S} is the mean of the spectrum. In this expression each summation is over the indices i which give non-zero values for both $S(v_i)$ and $S(v_i + \Delta\nu)$ (that is, we only

include the ‘good’ data in the auto-correlation analysis). The ACF calculated using equation (1) is shown in Extended Data Fig. 7.

The central part of the ACF (for lags in the range -1.016 to $+1.016$ MHz) after removing the zero lag was then fitted with a Lorentzian function⁴⁹ of the form:

$$\frac{a}{x^2 + (\Delta\nu_d)^2} + b \quad (2)$$

using a least-squares fit, for free parameters: amplitude a ; the decorrelation bandwidth (also known as the scintillation bandwidth) $\Delta\nu_d$, defined⁴⁸ as the half-width at half-maximum of the ACF; and offset b . Extended Data Fig. 7 shows the fit to the ACF. The Lorentzian fit, with 127 degrees of freedom, returned a χ^2 of 105.2. We assume that the ACF between 3 MHz and 20 MHz lags contains no structure and represents the noise in the central profile of the ACF. We measure the standard deviation in this region and use this as our uncertainty for the calculation of χ^2 . The P value of the fit is 0.92.

We measure the scintillation bandwidth to be $59 \pm 13 \text{ kHz}$. This estimate is consistent with the NE2001 model⁵⁰ prediction of about 60 kHz along the line-of-sight at our observing frequency of 1.7 GHz. Using the simple relationship

$$2\pi\tau\Delta\nu_d \approx 1 \quad (3)$$

we estimate a scattering timescale τ of about $2.7 \mu\text{s}$, which we find is also similar to the NE2001 model prediction of around $2 \mu\text{s}$ along the line of sight⁵⁰. This constraint on the scattering time is much tighter compared to CHIME/FRB measurements⁶ of FRB 180916.J0158+65 bursts, even after accounting for the different observing frequencies and the typical v^{-4} scaling of scattering time. CHIME/FRB nominally measured scattering times of approximately 2 ms for two FRB 180916.J0158+65 bursts, but these measurements are probably a reflection of burst morphology as opposed to genuine scattering effects (as was previously considered⁶).

High-time-resolution correlation and burst imaging

Coherently dedispersed visibilities for each burst were created by re-correlating the EVN data for only the time ranges corresponding to the burst durations. The exact time ranges were initially determined from the Effelsberg PSRIX data and then refined using coherently dedispersed Effelsberg auto-correlations. From the resulting auto-correlations we created pulse profiles and used these to set the optimal correlator gates applied to the interferometric data.

The a priori position of FRB 180916.J0158+65 provided at the time of the EVN observation had an uncertainty of about 3 arcmin (see above), making it infeasible to localize the bursts by directly imaging this region at milli-arcsecond resolution (which would require an image with around 10^{11} pixels). However, for strong signals, it is possible to estimate the position of the source from the geometric delays across the different telescope baselines. The differential geometric phase delay $\Delta\phi_g$ of the source with respect to the phase centre (a priori pointing position) for a given baseline is given by^{51,52}:

$$\Delta\phi_g = 2\pi\nu(u\Delta\alpha\cos\delta + v\Delta\delta) \quad (4)$$

where ν is the observed frequency, $(\Delta\alpha, \Delta\delta)$ is the positional offset of the source with respect to the phase centre in right ascension (α) and declination (δ), respectively, and (u, v) are the coordinate offsets for the given baseline.

We used the strongest burst, B4, to estimate the offset of the source with respect to the phase centre. We then re-correlated the data at this refined J2000 position of $\alpha = 01 \text{ h } 58 \text{ min } 00.5 \text{ s}$, $\delta = 65^\circ 43' 01.0''$ (with an estimated uncertainty of a few arcseconds), which was around 2 arcmin from the a priori position—and thus consistent within the

estimated uncertainties. We applied the previously described EVN calibration to these burst data and imaged the individual bursts. All bursts were detected above a 7σ confidence level. Different imaging schemes were used during the imaging process in order to emphasize resolution (that is, contribution from the longest baselines) or sensitivity (that is, contribution from the core of the array). The final images were produced by using a natural weighting and excluding data from the Tianma station which, despite providing the highest resolution, exhibited potential calibration issues that could affect the absolute burst positions by a few milli-arcseconds—especially for such short integration times, where the uv coverage is poor. Table 1 lists the burst properties obtained from the EVN images, which are shown in Fig. 2. An image of the combined burst data was also produced. This final image is dominated by the emission of the strongest burst, B4, and thus we only consider the results from the four bursts individually.

The flux densities and positions were measured using Difmap and the Common Astronomy Software Applications (CASA) software packages by fitting a circular Gaussian distribution component to the detected emission in the uv plane, which is expected to be a robust method against station gain calibration uncertainties⁵³. The position of each burst was measured independently and then we determined a weighted average J2000 position for the source of $\alpha = 01^{\text{h}} 58^{\text{min}} 00.75017^{\text{s}} \pm 2.3$ mas, $\delta = 65^{\circ} 43' 00.3152'' \pm 2.3$ mas, where we used the fluence of each burst as weights. This is within 1.7 arcsec of the position determined via mapping the geometric delays. The final positional uncertainty reflects the statistical uncertainties from the individual position measurements (about 1 mas), the uncertainties in the absolute International Celestial Reference Frame position of the phase calibrator (J0207+6246; 0.15 mas) and check source (J0140+6346; 0.1 mas), and the systematic uncertainty associated with the phase-referencing technique and the extended structure of the check source and phase calibrator (around 2 mas), as explained previously. Uncertainties were added in quadrature.

Finally, we searched for continuum radio counterparts of FRB 180916.J0158+65 by imaging the full interferometric dataset with a field-of-view of $2 \text{ arcsec} \times 2 \text{ arcsec}$ centred at the position of the bursts (and thus also covering the full extent of the nearby star-forming region). We detected no emission at the position of FRB 180916.J0158+65 as well as no significant ($>4.5\sigma$) compact emission anywhere in the field above the r.m.s. noise level of $10 \mu\text{Jy}$ per beam ($19 \mu\text{Jy}$ per beam when excluding the data from the Tianma station). We also searched for possible emission from the core of the galaxy, but found no signal above the 6σ r.m.s. noise level in a $4 \text{ arcsec} \times 4 \text{ arcsec}$ area.

VLA observations

In June 2019, we used the VLA to perform a quasi-simultaneous search for millisecond transients and faint persistent emission associated with FRB 180916.J0158+65. The VLA observed from 1 GHz to 2 GHz with baseline lengths up to 11 km, giving a synthesized beam size of roughly 4 arcsec. VLA visibilities were sampled at 5-ms time resolution and searched in real time by the Realfast system⁵⁴; the same data were integrated at 3-s time resolution and calibrated with the standard CASA calibration pipeline. In a total of 14 h of observing (with on-target efficiency of 80%), we found no millisecond transients to an 8σ limit of approximately 50 mJy per beam in 5 ms or, equivalently, a fluence limit of $0.25 \mu\text{Jy ms}$. No VLA observing was coincident with known burst times detected by the EVN. We concatenated all 14 h of data, applied an iteration of phase self-calibration using relatively bright background sources in the field of view of the antennas, and imaged 600 MHz of the bandwidth centred near 1.6 GHz to search for persistent radio emission on arcsecond scales. We confirmed that the astrometric accuracy of the deep image is good to better than 1 arcsec by associating seven bright field radio sources to the catalogued location in the NRAO VLA Sky Survey⁵⁵. No persistent emission is detected at the position of FRB 180916.J0158+65 brighter than a 3σ limit of $18 \mu\text{Jy}$ per beam. A $25\text{-}\mu\text{Jy}$ source is located at a nearby J2000 position of $\alpha = 01^{\text{h}} 58^{\text{min}} 00.9^{\text{s}}$,

$\delta = 65^{\circ} 43' 07''$ (see Extended Data Fig. 2), but this position is offset by approximately 7 arcsec from the location of FRB 180916.J0158+65, which is much more than the astrometric precision, estimated to be 0.4 arcsec (the VLA observed in its B configuration at the time). It is thus very unlikely to be associated with FRB 180916.J0158+65 or the host galaxy.

Optical observations and host galaxy

The EVN localization of FRB 180916.J0158+65 places it at the outskirts of SDSS J015800.28+654253.0, an apparent Sb spiral galaxy (possibly with a faint bar) with an estimated¹⁵ photometric redshift $z_{\text{phot}} = 0.07 \pm 0.05$.

We obtained imaging and spectroscopic observations of the host galaxy using the GMOS spectrograph on the Gemini-North telescope between July and September 2019 (programme ID GN-2019A-DD-110). We acquired $2 \times 900\text{-s}$ exposures with each of the g' and r' filters. The images were processed with the Gemini IRAF/pyraf package, and sources were extracted using SExtractor⁵⁶. The images were de-warped and astrometrically corrected by matching the point source positions to those from the Gaia Data Release 2 (DR2) Catalogue^{57,58}. The matching precision was 17–20 mas r.m.s. for each image. The seeing was measured to be 0.99 and 0.78 arcsec in the g' and r' images, respectively.

Figure 3 shows the r' image of the galaxy, along with the position of FRB 180916.J0158+65. The galaxy is nearly face-on, with spiral arm structures visible. FRB 180916.J0158+65 appears to be co-located with one of the outer arms of the galaxy, near a bright clump in the r' image (see Extended Data Fig. 4 for a more detailed zoom on this region). We attribute this emission to that of H α , which is bright in emission in the GMOS spectra and, at the redshift of the host galaxy, falls within the r' image. The total stellar mass of the galaxy has been estimated to be about 10^{10} times the mass of the Sun by using the WISE W1 and W2 colours⁵⁹, which provide a more robust estimation given that they are less affected by extinction.

We performed long-slit optical spectroscopy, simultaneously targeting the galaxy core and the FRB location, in order to measure the redshift and spectral properties of the galaxy and the location of FRB 180916.J0158+65. We acquired $4 \times 900\text{-s}$ spectroscopic observations with a 1.5-arcsec slit and the R400 grating—along with corresponding flat fields, copper–argon arcs, and observations of BD+28 4211 to correct for sensitivity and extinction. As shown in Extended Data Fig. 4, the slit was rotated to align with the host galaxy centre and FRB position.

The spectroscopic data were processed with the Gemini IRAF/pyraf package. The FWHM of the emission lines from the sky was measured to be $7\text{--}8 \text{ \AA}$, matching the theoretical resolving power of $R \approx 640$. The wavelength calibration with copper–argon emission lines had a precision of $0.7\text{--}0.8 \text{ \AA}$. However, the lack of arc lines towards the bluer edge reduces the accuracy of the wavelength solution towards $5,200 \text{ \AA}$.

We extracted the spectrum within 5 arcsec of the galaxy centre as well as 2 arcsec around the location of FRB 180916.J0158+65 itself. We used the trace of the galaxy centre, offset by 7.7 arcsec to trace the location of FRB 180916.J0158+65. Figure 3 shows the calibrated spectra at each location separately. We identify redshifted H α , N II, S II and O III lines with an average redshift of $z = 0.033 \pm 0.001$ if all lines are included and $z = 0.0337 \pm 0.0002$ when excluding the O III lines that are at the blue edge of the charge-coupled device (CCD)—and which hence may have reduced wavelength calibration accuracy. Extended Data Table 2 shows the line centroids, widths and fluxes. The spectrum at the location of FRB 180916.J0158+65 is dominated by emission lines with little continuum emission. The O III 5,007 \AA line is detected at the FRB location but was corrupted by a cosmic-ray hit. As the slit was positioned at the edge of the nearby star-forming clump, we observe a non-uniform slit illumination pattern and the line centroids, especially for H α , are shifted towards the redder wavelengths by about 1 \AA . Nevertheless, we can confirm that both the clump and the galaxy are at the same distance.

The flux obtained for the H α emission at the position of FRB 180916.J0158+65 (which is dominated by the star-forming clump) implies a

Article

luminosity of $L_{\text{H}\alpha} \approx (2.0 \pm 0.1) \times 10^{39}$ erg s $^{-1}$, which corresponds to a star-formation rate⁶⁰ of about $0.016 M_{\odot}$ yr $^{-1}$. These values were extracted from a region of $1.5 \text{ arcsec} \times 2 \text{ arcsec}$ around the FRB, corresponding to 1.5 kpc^2 , implying a star-formation surface density of about $10^{-2} M_{\odot} \text{ yr}^{-1} \text{kpc}^{-2}$. Note that these values can be strongly affected by extinction, which is estimated to be $E(B - V) \approx 1.01$.

From the H α , N II and S II line fluxes, we estimate the metallicity of the galaxy⁶¹ to be $12 + \log(\text{O/H}) = 8.82$, close to solar neighbourhood metallicity, and five times higher when compared to the host of FRB 121102 (<8.1 on the same metallicity scale¹⁷).

Chance alignment probability with host galaxy

The projected position of FRB 180916.J0158+65 is coincident with a star-forming clump in the spiral galaxy SDSS J015800.28+654253.0. To confirm an association with the galaxy we have estimated the probability of chance coincidence between the two sources.

We have considered a uniform density of galaxies across the sky. Assuming a Poisson distribution of galaxies in the relevant co-moving volume, we estimate the number density of typical galaxies brighter than $M_B = -16$ (that is, galaxies with masses greater than about 40% of the dwarf galaxy host¹⁷ of FRB 121102) based on the all-galaxy luminosity function^{62,63}, and their typical size distribution based on the galaxies reported in SDSS DR7⁶⁴. Then, we calculate the chance coincidence probability for a source to be co-located within twice the median half-light radius of any galaxy as a function of redshift.

At the measured redshift of $z \approx 0.0337$, the chance coincidence probability $P \ll 0.1\%$. However, we may consider the probability up to a redshift of approximately 0.11, the maximum redshift considered for FRB 180916.J0158+65 based on the observed DM⁶. Even in this case $P < 1\%$ (see Extended Data Fig. 8). The association between FRB 180916.J0158+65 and the galaxy is thus statistically robust.

DM budget

FRB 180916.J0158+65 is close to the Galactic plane, with longitude $l = 129.7^\circ$ and latitude $b = 3.7^\circ$. The total measured DM of FRB 180916.J0158+65 is $\text{DM}_{\text{tot}} = 348.76 \text{ pc cm}^{-3}$, and is expected to be the sum of contributions from the Milky Way disk (DM_{MW}) and halo (DM_{halo}), the intergalactic medium (DM_{IGM}), and host galaxy (DM_{host} ; including both the ISM and halo of the host). For the line-of-sight to FRB 180916.J0158+65, DM_{MW} is predicted to be 199 pc cm^{-3} and 325 pc cm^{-3} by the NE2001 and YMW16 Galactic electron density models, respectively^{50,65}. DM_{halo} is estimated to be $50\text{--}80 \text{ pc cm}^{-3}$ or approximately 45 pc cm^{-3} , according to two available models^{12,66}. Given the range of model predictions, one can ascribe up to roughly 100 pc cm^{-3} to DM_{IGM} and DM_{host} . For redshift $z = 0.0337$, DM_{IGM} is expected to be⁶⁷ approximately 34 pc cm^{-3} —although this estimate is highly dependent on line of sight for low redshift⁶⁸. Overall, after subtracting these various contributions, DM_{host} is probably less than 70 pc cm^{-3} , and could be much smaller. The YMW16 model over-predicts DM_{MW} in this direction (unless the DM_{halo} , DM_{IGM} and DM_{host} contributions are all much smaller than expected), and this illustrates that FRB DMs will help constrain Galactic electron density models. Conversely, because the line of sight to FRB 180916.J0158+65 passes through the Galactic plane, with a large but uncertain Galactic DM contribution, it is unlikely to be a good probe for refining the DM-z relationship in the IGM⁶⁷.

Comparison with the other localized repeating FRB

The physical origin of the FRB phenomenon remains unclear, and many of the proposed models³ remain consistent with the observational facts we present here for FRB 180916.J0158+65. We now briefly consider the nature of FRB 180916.J0158+65 by comparison to two of the families of models proposed for FRB 121102, which is the FRB source studied in most detail to date, and the only other well localized repeater.

One of the models to explain the associated persistent radio counterpart to FRB 121102 proposes the existence of a 20–50-year-old supernova remnant and nebula powered by a young flaring magnetar^{22,23,69,70}.

The absence of a similarly bright radio nebula associated with FRB 180916.J0158+65 could be explained, in this model, as an older system whose emission has already faded. Assuming a similar model²², the upper limits on persistent radio emission associated with FRB 180916.J0158+65 are consistent with a system that is at least about five times older than FRB 121102, and thus at least 200–500 yr old. Additionally, the same model also predicts a characteristic decay of the RM with time. An RM as large as the one observed towards FRB 121102²¹ would drop to the RM observed⁶ towards FRB 180916.J0158+65 at a source age of about 300 yr. However, while the results we present here are conceivably consistent with the young magnetar scenario for repeating FRBs, we find no new support for this scenario.

Other models, inspired originally by FRB 121102, invoke interaction between a nearby strong plasma stream and a neutron star's magnetosphere⁷¹. In the case of FRB 121102, the large²¹ RM and the observational similarity¹⁴ of its compact, persistent radio source to low-luminosity active galactic nuclei suggest that the bursts could originate from a massive black hole, or a neutron star in the near vicinity. An accreting massive black hole can provide a plasma stream that could interact with a neutron star magnetosphere⁷². The absence of a persistent radio counterpart to FRB 180916.J0158+65, and its location in the spiral arm of a morphologically well defined galaxy, make such a model arguably less likely in the case of FRB 180916.J0158+65. For a black hole with a similar mass to that of the one considered for FRB 121102 ($10^5 M_{\odot}$ to $10^6 M_{\odot}$), our upper limits would imply a very low accretion rate of about $10^{-7} L_{\text{Edd}}$ where L_{Edd} is the Eddington luminosity. Nonetheless, this accretion rate is still compatible with the low end observed in low-luminosity active galactic nuclei⁷⁶. The presence of a massive black hole at the apex of the star-forming clump is thus not excluded, although rather unlikely. Nonetheless, in an interacting model⁷¹, the plasma stream can also have a different origin, and it is conceivable that FRB 180916.J0158+65 is a neutron star interacting with, for example, the jet of a stellar-mass black hole.

The proximity of FRB 180916.J0158+65 will aid in performing deep multi-wavelength observations, which may help to discriminate between the various scenarios outlined above, while potentially also suggesting new ones.

Data availability

The datasets generated from the EVN observations and analysed in this study are available at the Public EVN Data Archive (<http://www.jive.eu/select-experiment>) under the experiment code EM135C. The datasets generated from the Gemini observations are available at the Public Gemini Observatory Archive (<https://archive.gemini.edu>) with Program ID GN-2019A-DD-110.

Code availability

The codes used to analyse the data are available at the following sites: AIPS (<http://www.aips.nrao.edu/index.shtml>), CASA (<https://casa.nrao.edu>), Difmap (<ftp://ftp.astro.caltech.edu/pub/difmap/difmap.html>), IRAF (<http://ast.noao.edu/data/software>), PRESTO (<https://github.com/scottransom/presto>), and PSRCHIVE (<http://psrchive.sourceforge.net>). This research made use of APLpy, an open-source plotting package for Python hosted at <http://aplpy.github.com>, Astropy, a community-developed core Python package for Astronomy⁷⁷, and Matplotlib⁷⁸.

35. CHIME/FRB Collaboration. The CHIME fast radio burst project: system overview. *Astrophys. J.* **863**, 48 (2018).
36. Keimpema, A. et al. The SFXC software correlator for very long baseline interferometry: algorithms and implementation. *Exp. Astron.* **39**, 259–279 (2015).
37. Greisen, E. W. AIPS, the VLA, and the VLBA. In *Information Handling in Astronomy. Historical Vistas* (ed. Heck, A.) Vol. 285, 109 (Astrophysics and Space Science Library, 2003).
38. Shepherd, M. C., Pearson, T. J. & Taylor, G. B. DIFMAP: an interactive program for synthesis imaging. *Bull. Am. Astron. Soc.* **26**, 987–989 (1994).

39. Chatterjee, S. et al. Pulsar parallaxes at 5 GHz with the Very Long Baseline Array. *Astrophys. J.* **604**, 339–345 (2004).
40. Pradel, N., Charlton, P. & Lestrade, J. F. Astrometric accuracy of phase-referenced observations with the VLBA and EVN. *Astron. Astrophys.* **452**, 1099–1106 (2006).
41. Kirsten, F., Vlemmings, W., Campbell, R. M., Kramer, M. & Chatterjee, S. Revisiting the birth locations of pulsars B1929+10, B2020+28, and B2021+51. *Astron. Astrophys.* **577**, A111 (2015).
42. Ransom, S. M. *New Search Techniques for Binary Pulsars*. PhD thesis, Harvard Univ. <https://ui.adsabs.harvard.edu/abs/2001PhDT.....123R/abstract> (2001).
43. Michilli, D. et al. Single-pulse classifier for the LOFAR tied-array all-sky survey. *Mon. Not. R. Astron. Soc.* **480**, 3457–3467 (2018).
44. Michilli, D. & Hessels, J. W. T. SpS: Single-pulse Searcher. *Astrophys. Source Code Library* 1806. 013 (2018).
45. Hotan, A. W., van Straten, W. & Manchester, R. N. PSRCHIVE and PSRFITS: an open approach to radio pulsar data storage and analysis. *Publ. Astron. Soc. Aust.* **21**, 302–309 (2004).
46. Hessels, J. W. T. et al. FRB 121102 bursts show complex time-frequency structure. *Astrophys. J.* **876**, L23 (2019).
47. Law, C. J. et al. A multi-telescope campaign on FRB 121102: implications for the FRB population. *Astrophys. J.* **850**, 76 (2017).
48. Cordes, J. M., Weisberg, J. M. & Boriakoff, V. Small-scale electron density turbulence in the interstellar medium. *Astrophys. J.* **288**, 221–247 (1985).
49. Rickett, B. J. Radio propagation through the turbulent interstellar plasma. *Annu. Rev. Astron. Astrophys.* **28**, 561–605 (1990).
50. Cordes, J. M. & Lazio, T. J. W. NE2001. I. A new model for the galactic distribution of free electrons and its fluctuations. Preprint at <https://arxiv.org/abs/astro-ph/0207156> (2002).
51. Fomalont, E. B. & Perley, R. A. Calibration and editing. In *Synthesis Imaging in Radio Astronomy II* (eds Taylor, G. B., Carilli, C. L. & Perley, R. A.) Vol. 180, 79 (Astronomical Society of the Pacific Conference Series, 1999).
52. Thompson, A. R. Fundamentals of Radio Interferometry. In *Synthesis Imaging in Radio Astronomy II* (eds Taylor, G. B., Carilli, C. L. & Perley, R. A.) Vol. 180, 11 (Astronomical Society of the Pacific Conference Series, 1999).
53. Natarajan, I. et al. Resolving the blazar CGRaBS J0809+5341 in the presence of telescope systematics. *Mon. Not. R. Astron. Soc.* **464**, 4306–4317 (2017).
54. Law, C. J. et al. realfast: real-time, commensal fast transient surveys with the Very Large Array. *Astrophys. J. Suppl.* **236**, 8 (2018).
55. Condon, J. J. et al. The NRAO VLA sky survey. *Astron. J.* **115**, 1693–1716 (1998).
56. Bertin, E. & Arnouts, S. SExtractor: software for source extraction. *Astron. Astrophys. Suppl. Ser.* **117**, 393–404 (1996).
57. Gaia Collaboration. Gaia Data Release 1. Summary of the astrometric, photometric, and survey properties. *Astron. Astrophys.* **595**, A2 (2016).
58. Gaia Collaboration. Gaia Data Release 2. Summary of the contents and survey properties. *Astron. Astrophys.* **616**, A1 (2018).
59. Jarrett, T. H. et al. Galaxy and Mass Assembly (GAMA): exploring the WISE web in G12. *Astrophys. J.* **836**, 182 (2017).
60. Kennicutt, J., Robert, C., Tamblyn, P. & Congdon, C. E. Past and future star formation in disk galaxies. *Astrophys. J.* **435**, 22 (1994).
61. Dopita, M. A., Kewley, L. J., Sutherland, R. S. & Nicholls, D. C. Chemical abundances in high-redshift galaxies: a powerful new emission line diagnostic. *Astrophys. Space Sci.* **361**, 61 (2016).
62. Faber, S. M. et al. Galaxy luminosity functions to $z = 1$ from DEEP2 and COMBO-17: implications for red galaxy formation. *Astrophys. J.* **665**, 265–294 (2007).
63. Blanton, M. R. et al. The galaxy luminosity function and luminosity density at redshift $z = 0.1$. *Astrophys. J.* **592**, 819–838 (2003).
64. Zhang, Y.-C. & Yang, X.-H. Size distribution of galaxies in SDSS DR7: weak dependence on halo environment. *Res. Astron. Astrophys.* **19**, 006 (2019).
65. Yao, J. M., Manchester, R. N. & Wang, N. A new electron-density model for estimation of pulsar and FRB Distances. *Astrophys. J.* **835**, 29 (2017).
66. Yamasaki, S. & Totani, T. The galactic halo contribution to the dispersion measure of extragalactic fast radio bursts. Preprint at <https://arxiv.org/abs/1909.00849> (2019).
67. Inoue, S. Probing the cosmic reionization history and local environment of gamma-ray bursts through radio dispersion. *Mon. Not. R. Astron. Soc.* **348**, 999–1008 (2004).
68. Li, Y., Zhang, B., Nagamine, K. & Shi, J. The FRB 121102 host is atypical among nearby fast radio bursts. *Astrophys. J.* **884**, L26 (2019).
69. Lyubarsky, Y. A model for fast extragalactic radio bursts. *Mon. Not. R. Astron. Soc.* **442**, L9–L13 (2014).
70. Beloborodov, A. M. A flaring magnetar in FRB 121102? *Astrophys. J.* **843**, L26 (2017).
71. Zhang, B. A “cosmic comb” model of fast radio bursts. *Astrophys. J.* **836**, L32 (2017).
72. Zhang, B. FRB 121102: a repeatedly combed neutron star by a nearby low-luminosity accreting supermassive black hole. *Astrophys. J.* **854**, L21 (2018).
73. Kewley, L. J., Dopita, M. A., Sutherland, R. S., Heisler, C. A. & Trevena, J. Theoretical modeling of starburst galaxies. *Astrophys. J.* **556**, 121–140 (2001).
74. Kewley, L. J. & Dopita, M. A. Using strong lines to estimate abundances in extragalactic H II regions and starburst galaxies. *Astrophys. J. Suppl.* **142**, 35–52 (2002).
75. Kauffmann, G. et al. The host galaxies of active galactic nuclei. *Mon. Not. R. Astron. Soc.* **346**, 1055–1077 (2003).
76. Loewenstein, M., Mushotzky, R. F., Angelini, L., Arnaud, K. A. & Quataert, E. Chandra limits on X-ray emission associated with the supermassive black holes in three giant elliptical galaxies. *Astrophys. J.* **555**, L21–L24 (2001).
77. Astropy Collaboration. Astropy: a community Python package for astronomy. *Astron. Astrophys.* **558**, A33 (2013).
78. Hunter, J. D. Matplotlib: a 2D graphics environment. *Comput. Sci. Eng.* **9**, 90–95 (2007).

Acknowledgements We thank W. J. G. de Blok, L. Connor, N. Maddox, E. Petroff, H. Vedantham and J. Weisberg for discussions. The European VLBI Network is a joint facility of independent European, African, Asian, and North American radio astronomy institutes. Scientific results from data presented in this publication are derived from the following EVN project code: EM135. This work was also based on simultaneous EVN and PSRIX data recording observations with the 100-m telescope of the Max-Planck-Institut für Radioastronomie at Effelsberg, and we thank the local staff for this arrangement. Our work is also based on observations obtained at the Gemini Observatory (programme DT-2019A-135), which is operated by the Association of Universities for Research in Astronomy, Inc., under a cooperative agreement with the NSF on behalf of the Gemini partnership: the National Science Foundation (United States), the National Research Council (Canada), CONICYT (Chile), Ministerio de Ciencia, Tecnología e Innovación Productiva (Argentina), and Ministério da Ciência, Tecnologia e Inovação (Brazil). B.M. acknowledges support from the Spanish Ministerio de Economía y Competitividad (MINECO) under grants AYA2016-76012-C3-1-P and MDM-2014-0369 of ICCUB (Unidad de Excelencia “María de Maeztu”). J.W.T.H. acknowledges funding from an NWO Vidi fellowship and from the European Research Council under the European Union’s Seventh Framework Programme (FP/2007-2013)/ERC Starting Grant agreement number 337062 (“DRAGNET”). M.B. is supported by an FRQNT Doctoral Research Award, Physics Department Excellence Award and a Mitacs Globalink Graduate Fellowship. R.K. is supported by ERC synergy grant number 610058 (“BlackHoleCam”). V.M.K. holds the Lorne Trottier Chair in Astrophysics and Cosmology, a Canada Research Chair and the R. Howard Webster Foundation Fellowship of CIFAR. V.M.K. receives support from an NSERC Discovery Grant and Herzberg Award, and from the FRQNT Centre de Recherche en Astrophysique du Québec. C.J.L. acknowledges support from NSF grant 1611606. D.M. is a Banting Fellow. K.A. acknowledges support from NSF grant AAG-1714897. B.A. is supported by a Chalk-Rowles Fellowship. A.M.A. acknowledges funding from an NWO Veni fellowship. S.B.-S. acknowledges support from NSF grant AAG-1714897. F.K. thanks the Swedish Research Council. U.-L.P. receives support from the Ontario Research Fund Research Excellence Program (ORF-RE), NSERC, the Simons Foundation, Thoth Technology Inc., and the Alexander von Humboldt Foundation. Z.P. is supported by a Schulich Graduate Fellowship. P.S. is a Dunlap Fellow and an NSERC Postdoctoral Fellow. The Dunlap Institute is funded through an endowment established by the David Dunlap family and the University of Toronto. K.M.S. is supported by an NSERC Discovery Grant, an Ontario Early Researcher Award, and a CIFAR fellowship. Part of this research was carried out at the Jet Propulsion Laboratory, California Institute of Technology, under a contract with the National Aeronautics and Space Administration. The NANOGRAv project receives support from National Science Foundation (NSF) Physics Frontiers Center award number 1430284. FRB research at the University of British Columbia (UBC) is supported by an NSERC Discovery Grant and by the Canadian Institute for Advanced Research. The CHIME/FRB baseband system is funded in part by a Canada Foundation for Innovation John R. Evans Leaders Fund award to I.H.S. The National Radio Astronomy Observatory (NRAO) is a facility of the National Science Foundation operated under cooperative agreement by Associated Universities, Inc. The Astronomical Image Processing System (AIPS) is a software package produced and maintained by NRAO. The Common Astronomy Software Applications (CASA) package is software produced and maintained by NRAO.

Author contributions B.M. is the Principal Investigator of the EVN observing programme and led the radio imaging analysis of those data. K.N. discovered the radio bursts and led the time-domain analysis. J.W.T.H. guided the time-domain analysis and made major contributions to the writing of the manuscript. S.P.T. and C.G.B. led the optical imaging and spectroscopic analyses. Z.P. performed an independent analysis of the EVN data, and in previous years pioneered the development of the EVN’s capabilities for fast transient research. A.K. created the software used to correlate the EVN baseband data. M.B. analysed the chance coincidence probability. R.K. arranged the Effelsberg PSRIX observations. C.J.L. analysed the VLA imaging data. D.M. determined the CHIME/FRB baseband position. V.M.K. had an important coordination role, enabling these results to be gathered. All other co-authors contributed to the CHIME/FRB discovery of the source or the interpretation of the analysis results and the final version of the manuscript.

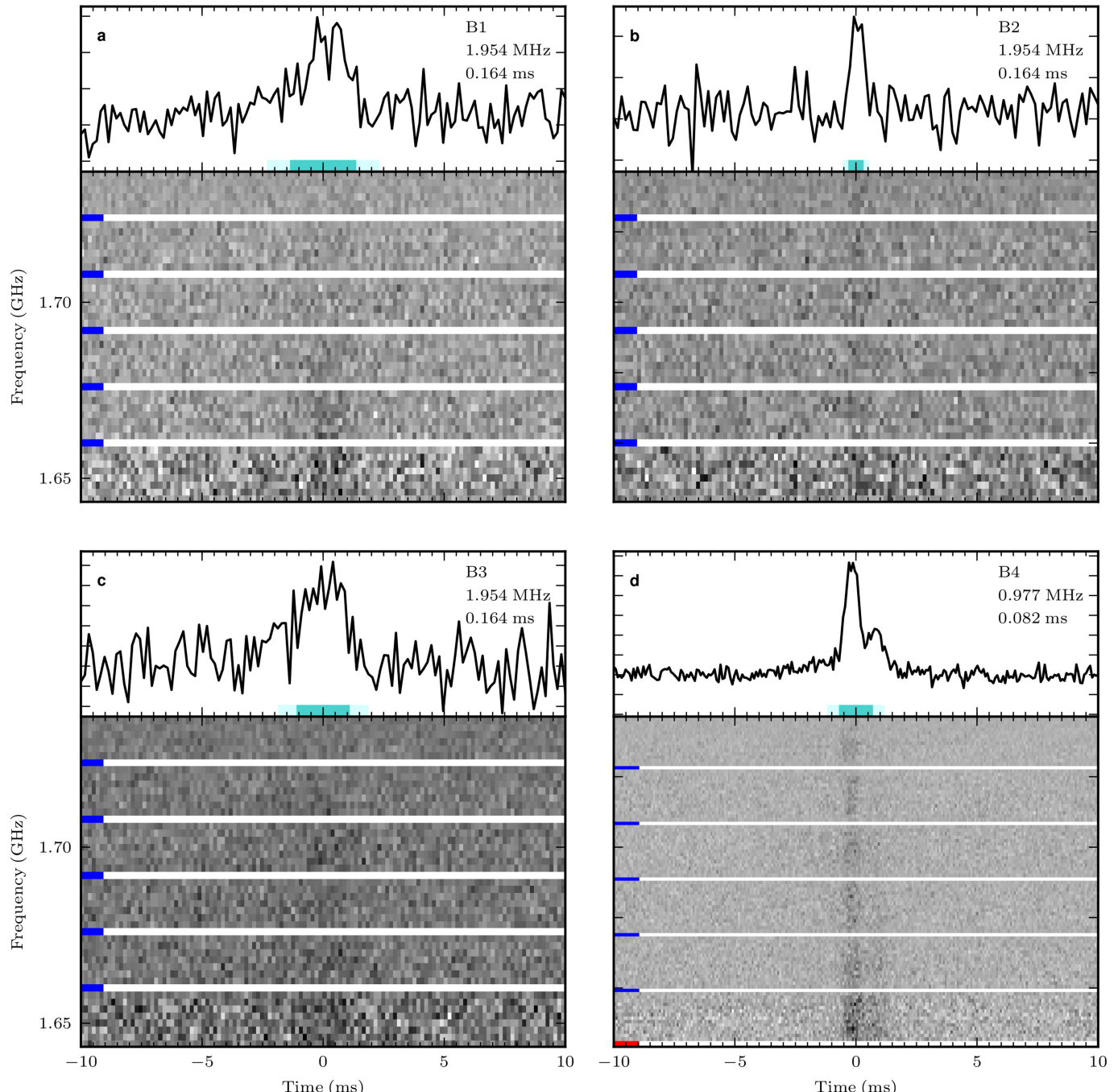
Competing interests The authors declare no competing interests.

Additional information

Correspondence and requests for materials should be addressed to J.W.T.H.

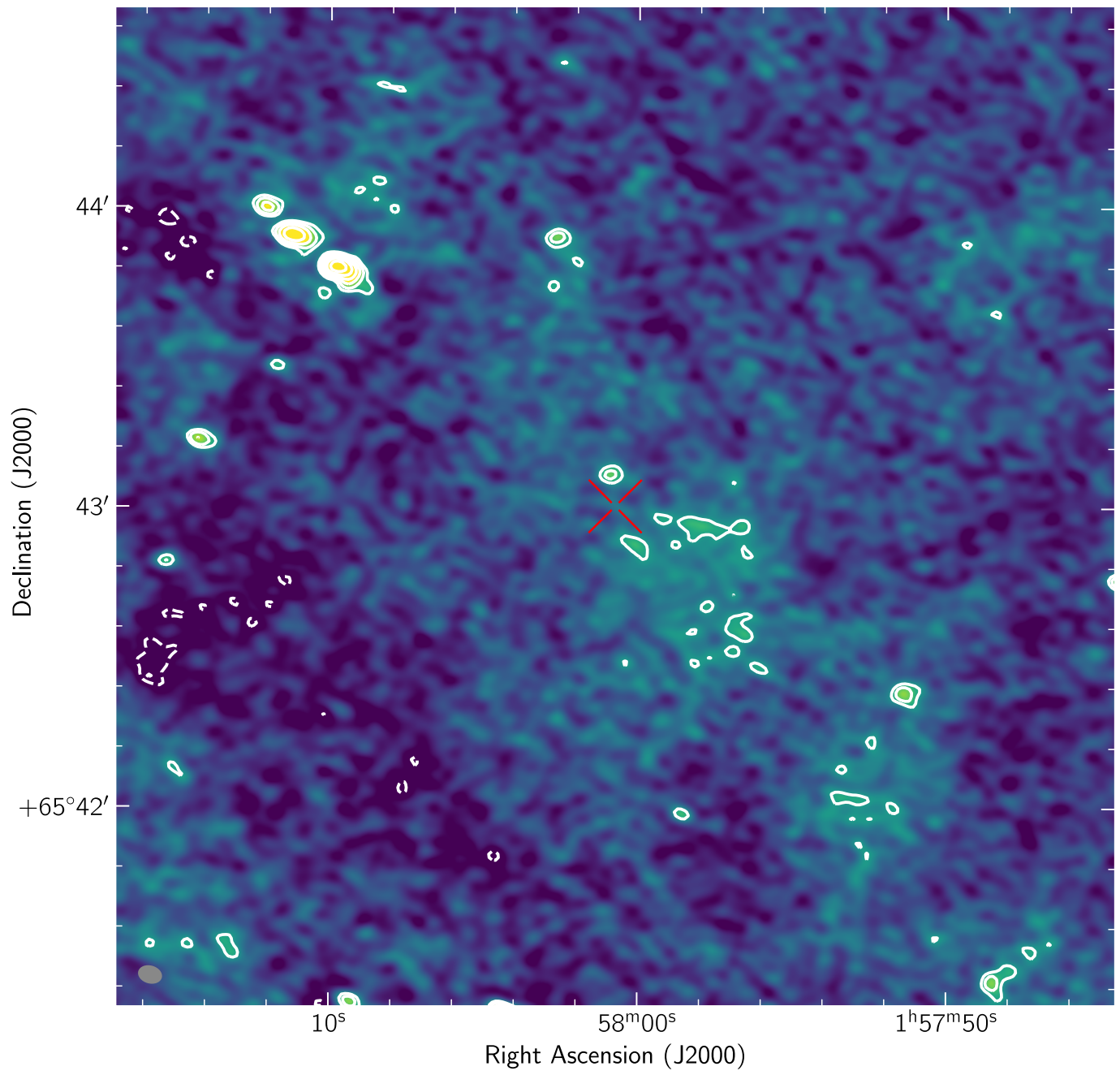
Peer review information *Nature* thanks Matthew Bailes and the other, anonymous, reviewer(s) for their contribution to the peer review of this work.

Reprints and permissions information is available at <http://www.nature.com/reprints>.



Extended Data Fig. 1 | Burst detections in Effelsberg PSRIX data. Band-averaged profiles and dynamic spectra of the four bursts, as detected in the PSRIX data (**a**, **b**, **c** and **d**). A 20-ms time window is shown surrounding the burst centre. Each burst was fitted with a Gaussian distribution to determine the FWHM duration, which is represented by the cyan bars. The lighter cyan encloses the 2σ region. The solid white lines are frequency channels that have

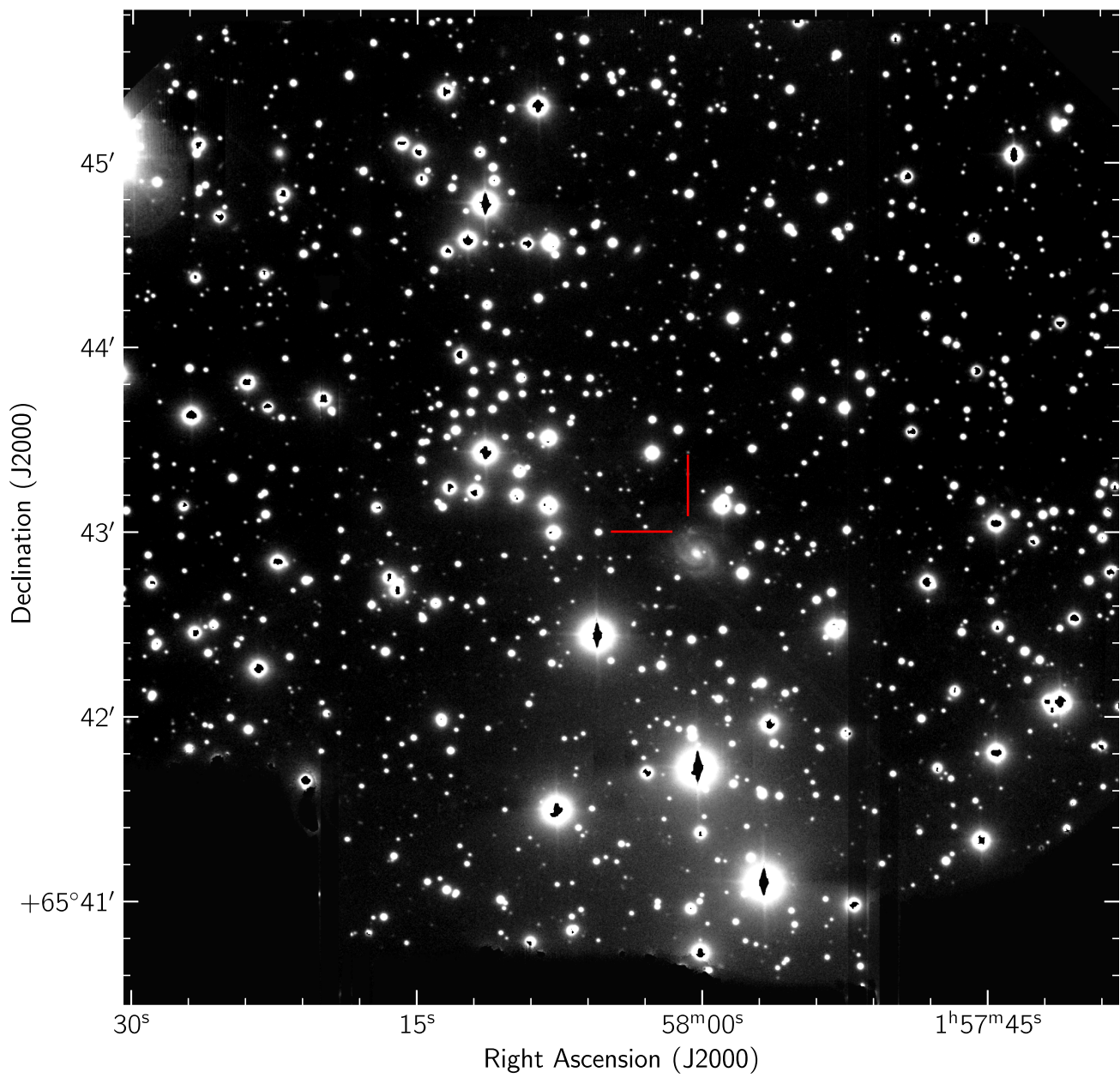
been removed from the data due to either RFI or subband edges, indicated by the red and blue markers, respectively. For visual clarity, bursts B1, B2 and B3 (**a**, **b** and **c**) are downsampled in both time and frequency by a factor of two. The RFI excision was done before downsampling. The time and frequency resolution used for plotting is shown in the top right of each panel.



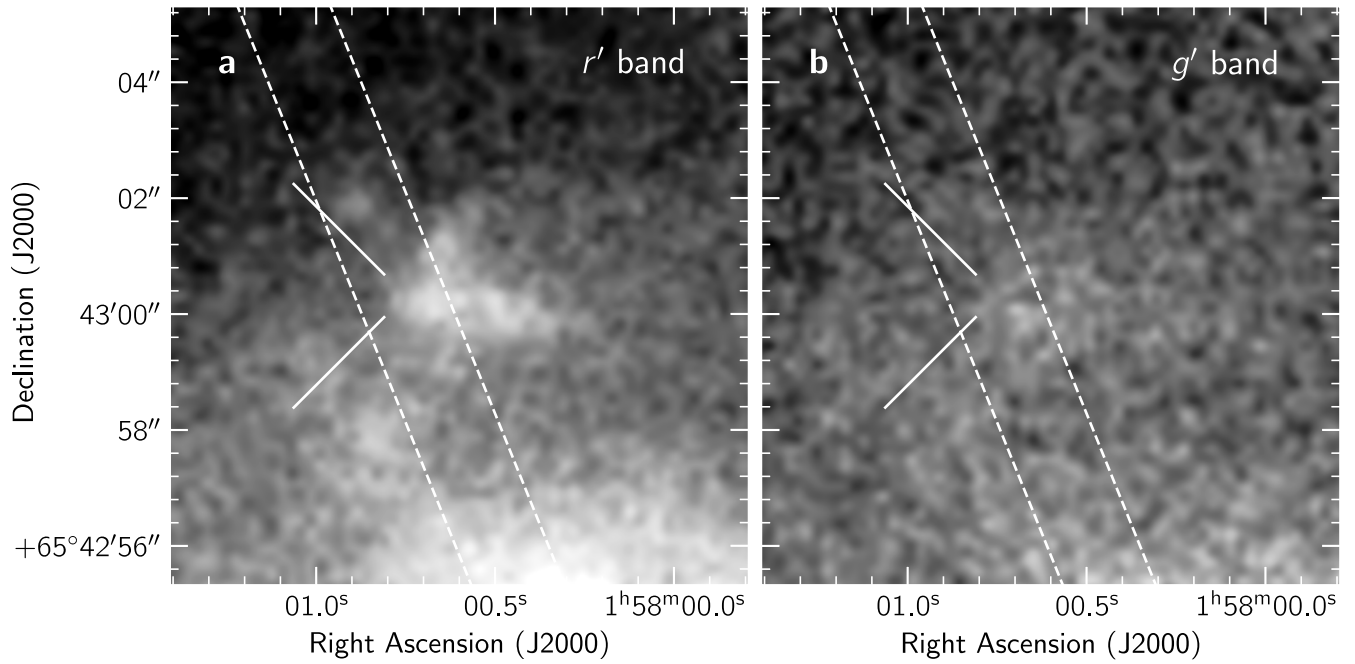
Extended Data Fig. 2 | VLA field image. Field of the continuum radio emission around FRB 180916.J0158+65 as seen by the VLA at 1.6 GHz with a bandwidth of 0.6 GHz. The position of FRB 180916.J0158+65 is marked by the red cross at the centre of the image. Contours start at the 3σ r.m.s. noise level of $18 \mu\text{Jy}$ per beam and increase by factors of $\sqrt{2}$. The synthesized beam is represented by

the grey ellipse in the bottom-left corner. Note that a faint source is detected at around 6 arcsec north of FRB 180916.J0158+65, but its separation is significant ($>3\sigma$ confidence level) and we thus conclude that it is not associated with FRB 180916.J0158+65.

Article

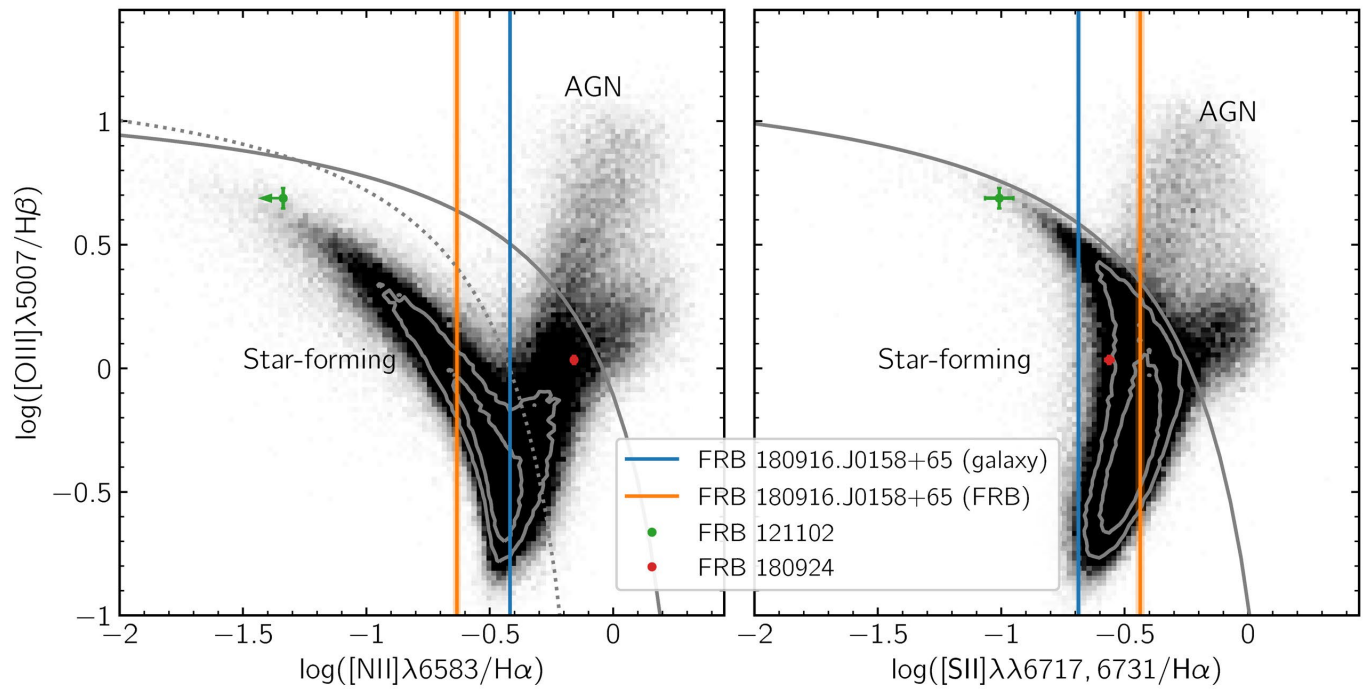


Extended Data Fig. 3 | Full field of view of the Gemini *r'* filter. The position of FRB 180916.J0158+65 is highlighted by the red cross. Note that the spiral galaxy associated with FRB 180916.J0158+65 is the only clearly visible galaxy in the field.



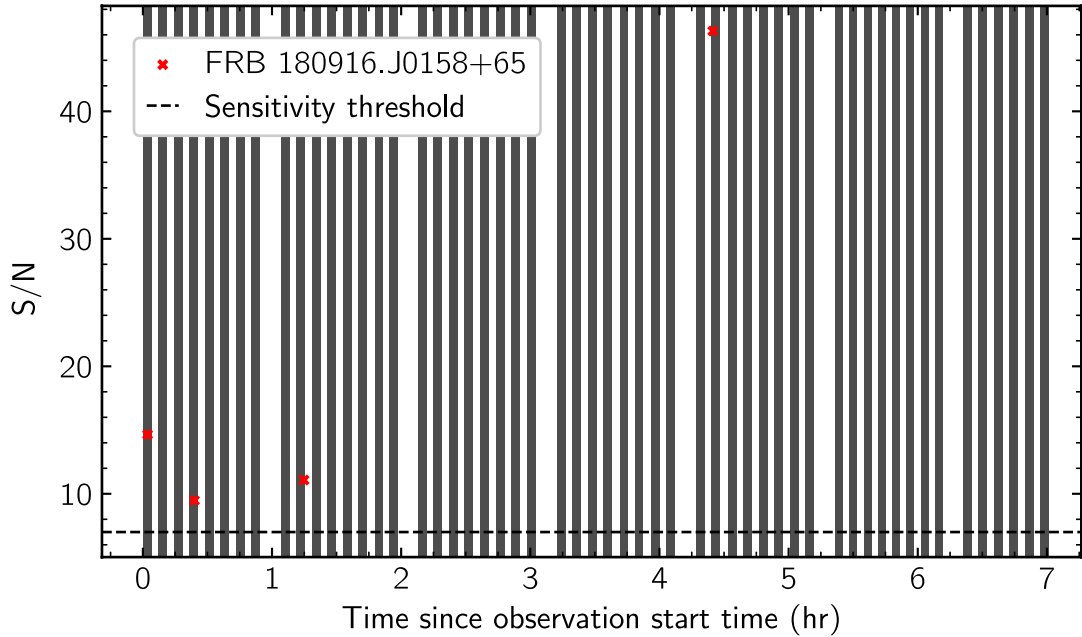
Extended Data Fig. 4 | Zoomed-in images at the position of FRB 180916.J0158+65. Gemini data at r' (a) and g' bands (b). The position of FRB 180916.J0158+65 is highlighted by the white cross. The uncertainty in its position is smaller than the resolution of these images. The dashed lines represent the

orientation and placement of the 1.5-arcsec spectroscopic slit used to obtain the optical spectra. Note that the slit does not cover the full star-forming region but the region centred on FRB 180916.J0158+65, and that the whole region is strongly affected by extinction ($E(g-r)=1.73\pm 0.09$).



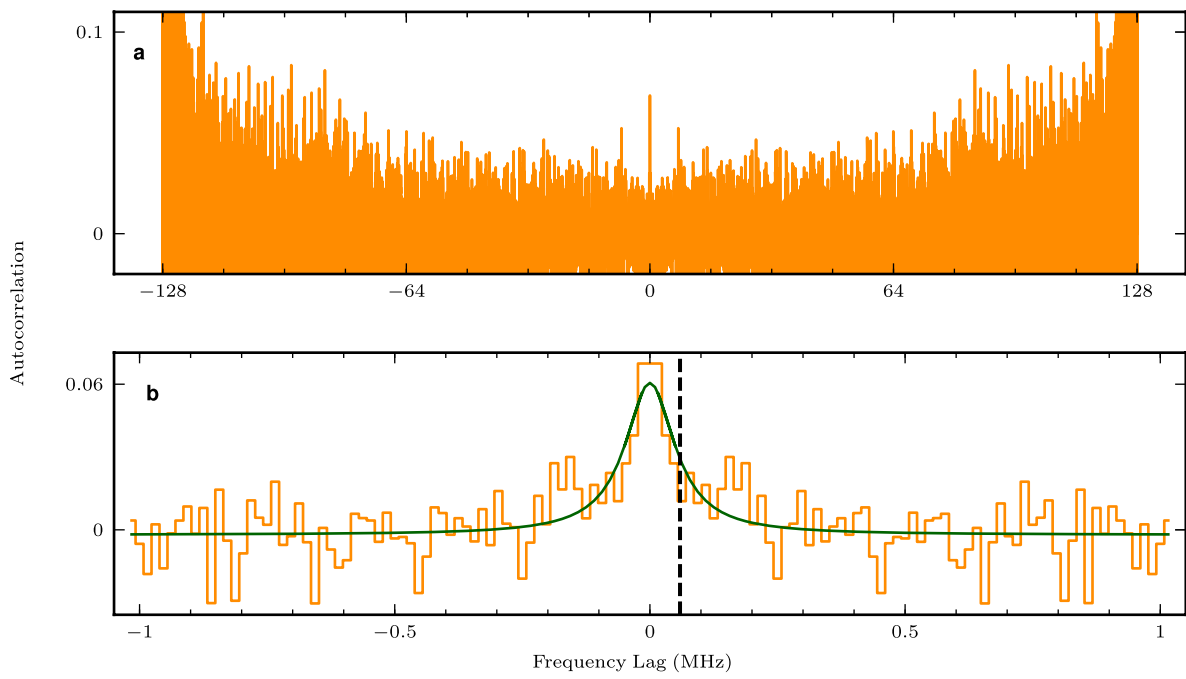
Extended Data Fig. 5 | Host galaxy source of ionization. Emission line flux ratios of [N II]/H α (left) and [S II]/H α (right) plotted against [O III]/H β . The greyscale distribution represents the SDSS DR12 sample¹⁵ of 240,000 galaxies that display significant emission lines ($>5\sigma$), where the solid and dotted grey lines denote the demarcations between star-forming and AGN-dominated galaxies^{73–75}. The host galaxies of FRB 121102 and FRB 180924 (shown by the

green and red circles, respectively, where error bars show the 1σ uncertainty) are consistent with star-forming and AGN-dominated galaxies, respectively^{11,17}. Though the Gemini-North spectrum of FRB 180916.J0158+65 does not cover the [O III] and H β lines, its [N II]/H α and [S II]/H α line ratios are broadly consistent with a star-formation-dominated galaxy (represented by the vertical lines and the 1σ region as linewidth).



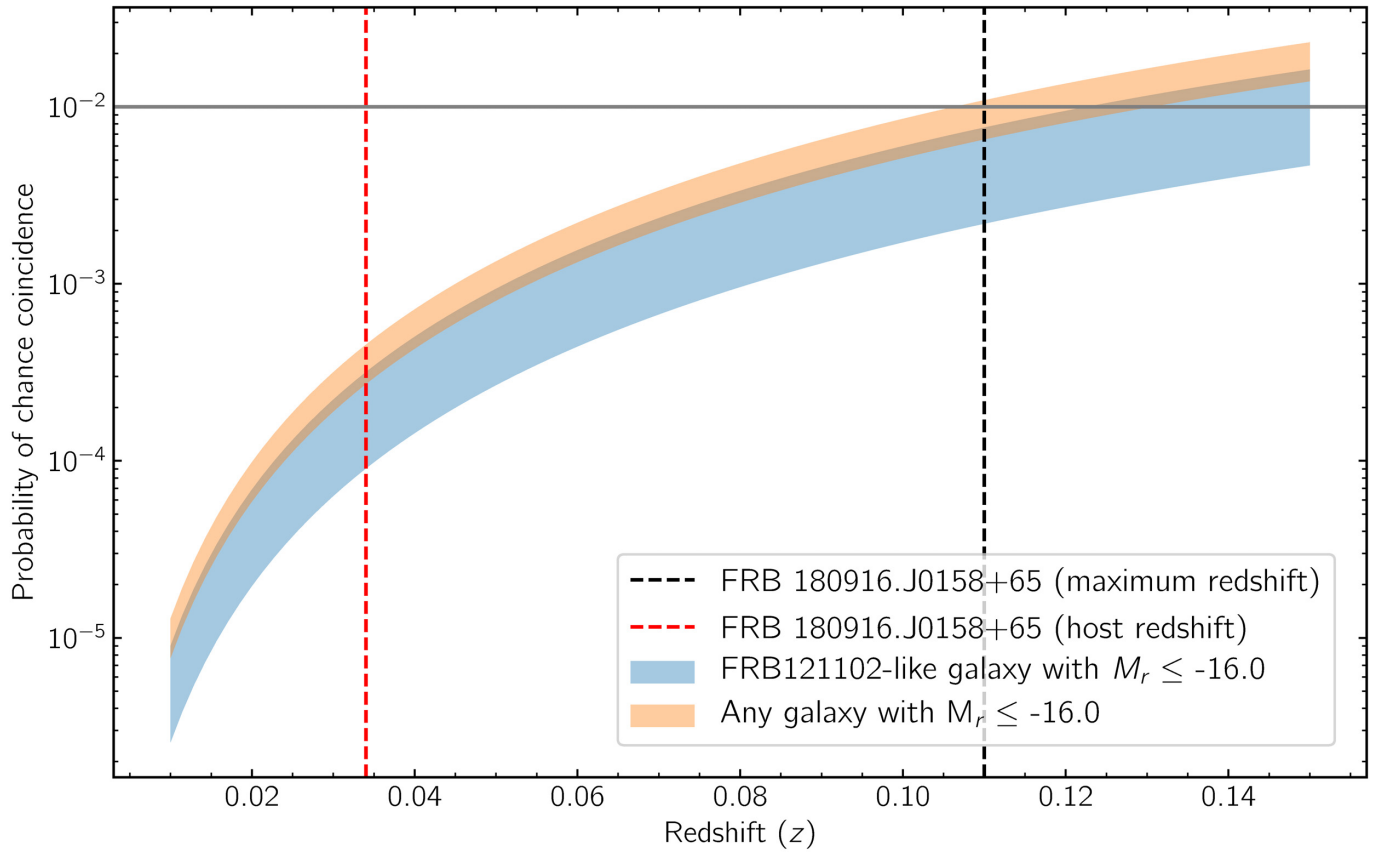
Extended Data Fig. 6 | Burst brightness and arrival times. Burst S/N as a function of time during our 2019 June 19 observation of FRB 180916.J0158+65. The grey bars represent scans of the FRB 180916.J0158+65 field. The red

crosses represent the four bursts (from left to right: B1, B2, B3, B4). The black dashed line indicates the detection threshold of our search in the pulsar-backend data ($S/N = 7$).



Extended Data Fig. 7 | Auto-correlation function and scintillation bandwidth of brightest burst, B4. **a.** The ACF of the spectrum of the bright, narrow burst component of burst B4. **b.** The ACF for lags between -1.016 MHz and $+1.016\text{ MHz}$. The zero-lag noise spike has been removed from the ACF.

A Lorentzian fit is shown in green in **b**. The black vertical dashed line represents the scintillation bandwidth, defined as the half width at half maximum of the Lorentzian fit.



Extended Data Fig. 8 | Redshift-cumulated probability of chance alignment coincidence. Probability of a chance alignment between FRB180916.J0158+65 and twice the median half-light radius of any galaxy with magnitude $M_B \leq -16$ (orange region) or with a dwarf galaxy like the host of FRB121102 (blue region) as a function of redshift. The horizontal grey line represents the 1% probability

threshold. At the redshift of the host galaxy, $z=0.0337$ (vertical dashed red line), the chance coincidence probability is $P \ll 0.1\%$, and at the maximum possible redshift of about 0.11 derived from the observed DM the probability is $<1\%$ (vertical dashed black line).

Article

Extended Data Table 1 | FRB 180916.J0158+65 burst properties as detected in both the Effelsberg PSRIX data and the Effelsberg auto-correlation data

Burst	Peak time ^a (MJD)	PSRIX data			Auto-correlations		
		S/N	DM (pc cm ⁻³)	Width (ms)	S/N	DM (pc cm ⁻³)	Width (ms)
B1	58653.0961366466	14.65	345	1.64	9.87	348.76	2.40
B2	58653.1112573504	9.48	349	0.33	9.61	348.76	0.32
B3	58653.1465969404	11.08	356	0.74	9.78	348.76	1.12
B4	58653.2785078914	46.30	350	0.49	65.42	348.76	0.06

S/N and width are determined using *single_pulse_search.py*, and are the exact values returned by this program for the best-fit boxcar function. The DM quoted for the PSRIX data are the DM corresponding to the optimal S/N detection. The DM for the Effelsberg auto-correlation data are 348.76 pc cm⁻³, which is the S/N optimizing DM found for the brightest burst, B4, using the PSRCHIVE tool *pdmp*.

^aTime of arrival (in Modified Julian Day, MJD) of the centre of the burst envelope at the Solar System barycentre after correcting to infinite frequency (that is, after removing the time delay from dispersion) using a DM of 348.76 pc cm⁻³.

Extended Data Table 2 | Properties of the spectral emission lines

Line ID	Galaxy Core			FRB Location		
	Centroid	Width	Flux	Centroid	Width	Flux
	(Å)	(Å)	(10^{-16} erg cm $^{-2}$ s $^{-1}$)	(Å)	(Å)	(10^{-16} erg cm $^{-2}$ s $^{-1}$)
O _{III} 4958.93 Å	5122.7	5.5	0.38(4)	—	—	—
O _{III} 5006.86 Å [†]	5155.6	5.6	4.76(4)	—	—	—
N _{II} 6548.05 Å	6767.9	5.5	0.31(4)	—	—	—
H α 6562.8 Å	6784.8	10.9	6.57(4)	6787.5	6.5	1.002(8)
N _{II} 6583.45 Å	6806.9	10.3	2.51(4)	6809.0	5.1	0.233(8)
S _{II} 6716.44 Å	6943.7	7.4*	0.77(4)	6946.2	6.4 ^{††}	0.243(5)
S _{II} 6730.81 Å	6953.8	7.4*	0.58(4)	6961.8	6.4 ^{††}	0.123(5)

Properties of the most relevant spectral lines observed at the location of the core of the galaxy and at the position of FRB 180916.J0158+65. Note that the fluxes are not corrected for extinction. Numbers in parentheses indicate 1 σ uncertainties in the least significant digits.

[†]The O III 5,006.86 Å line is detected at the FRB location but is corrupted by a cosmic-ray hit.

*,^{††}A single value of linewidth was fitted for both lines.